 doi:10.20944/preprints202211.0035.v1

Article

Self-Calibrating Magnetometer-Free Inertial Motion Tracking of 2-DoF Joints

Daniel Laidig [1,*], Ive Weygers [2] and Thomas Seel [2]

[1] Control Systems Group, Technische Universität Berlin, 10623 Berlin, Germany
[2] Department Artificial Intelligence in Biomedical Engineering, Friedrich-Alexander-Universität Erlangen-Nürnberg, 91052 Erlangen, Germany; thomas.seel@fau.de; ive.weygers@fau.de
* Correspondence: laidig@control.tu-berlin.de

Abstract: Human motion analysis using inertial measurement units (IMUs) has recently been shown to provide accuracy similar to the gold standard, marker-based optical motion capture, but at much lower costs and while being less restrictive and time-consuming. However, IMU-based motion analysis requires precise knowledge of the orientation in which the sensor is attached to the body segments. This knowledge is commonly obtained via an anatomical calibration procedure based on precisely defined poses or motions, which is time-consuming and error-prone. In the present work, we propose a self-calibrating approach for magnetometer-free joint angle tracking that is suitable for joints with two degrees of freedom (DoF), such as the elbow, ankle, and metacarpophalangeal finger joints. The proposed methods exploit kinematic constraints to simultaneously identify the joint axes and the heading offset. The experimental evaluation shows that the proposed methods are able to estimate plausible and consistent joint axes from just ten seconds of arbitrary elbow joint motion. Comparison with optical motion capture shows that the proposed methods yield joint angles with similar accuracy as a conventional IMU-based method while being much less restrictive. Therefore, the proposed methods improve the practical usability of IMU-based motion tracking in many clinical and biomedical applications.

Keywords: anatomical calibration; sensor-to-segment calibration; kinematic constraints; human motion analysis; elbow joint; inertial sensor; inertial measurement unit

1. Introduction

Marker-based optical motion capture (OMC) is considered the gold standard for human motion analysis. However, this method is time-consuming and confined to expensive laboratory environments. Ambulatory real-time motion analysis can be achieved at much lower costs with inertial measurement units (IMUs). Recent studies have shown that the accuracy of IMU-based motion analysis is comparable to marker-based OMC, see, e.g., [1,2].

However, in order to derive anatomically meaningful kinematic quantities, for example, joint angles, the orientation of each IMU with respect to its body segment must be known, as illustrated in Figure 1. Even small misalignments between the assumed and actual orientation of the IMUs on the body lead to errors in the obtained kinematic quantities. To ensure accurate motion tracking, it is therefore desirable to accurately determine this orientation.

In practice, this is often achieved by manual placement of the IMUs on the respective body segments in a specified orientation [3], which is error-prone, especially when the attachment of sensors is to be performed by patients or by non-medical personnel.

An alternative is to include a procedure that determines the orientation of each IMU with respect to its body segment based on data measured by the sensors. This procedure is called *anatomical calibration* or *sensor-to-segment calibration*, which is not to be confused with sensor calibration. Sensor calibration determines parameters such as scaling and bias in

Preprints (www.preprints.org) | NOT PEER-REVIEWED | Posted: 2 November 2022 doi:10.20944/preprints202211.0035.v1

order to increase the accuracy of the sensor orientation estimates. Anatomical calibration determines how the sensors are attached to the body segments to ensure that the rotation axes used for calculating joint angles match the anatomical axes of joint rotation.

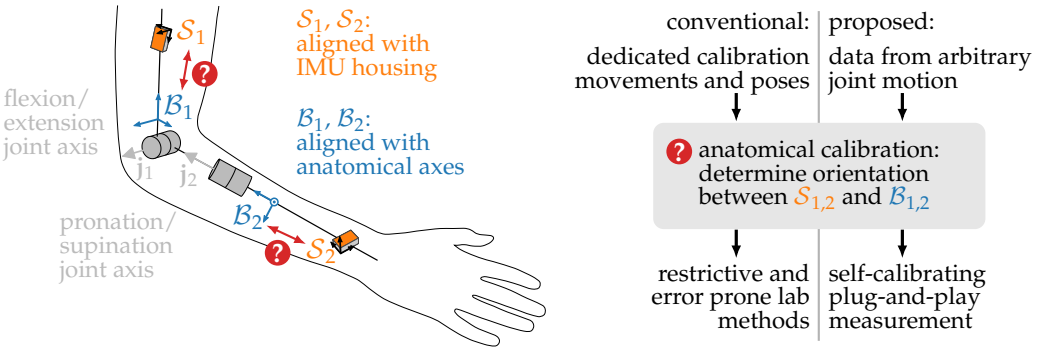

Figure 1. Anatomical calibration, also called sensor-to-segment calibration, is the task of determining how the IMUs are attached to the body segments. More precisely, the rotations between the IMU coordinate systems $\mathcal{S}_{1,2}$, defined by the sensor housing, and the corresponding body segments $\mathcal{B}_{1,2}$, determined by anatomical axes such as the joint axes $\mathbf{j}_{1,2}$, have to be determined. Conventional methods rely on precisely defined calibration movements and poses, whereas the proposed methods use kinematic constraints to derive this information from arbitrary joint motion.

As detailed in Section 2, anatomical calibration traditionally relies on precisely defined calibration poses or motions. Less restrictive approaches aim for anatomical calibration based on arbitrary joint motion. Such approaches have been proposed for (approximate) hinge joints [4,5]. In the following, we consider the more challenging case of joints with two degrees of freedom (DoF), such as the elbow joint, the metacarpophalangeal joints (MCP) of the finger, or the ankle joint. The present contribution introduces methods for self-calibrating joint angle tracking that

- use two kinematic constraints for 2-DoF joints, one for the angular rates (as already introduced in [6,7]) and a novel constraint for the relative segment orientations
- do not make use of magnetometer measurements and are therefore insensitive to magnetic disturbances (otherwise, temporary magnetic disturbances could permanently deteriorate accuracy until calibration is repeated)
- instead simultaneously estimate the heading offset to facilitate magnetometer-free joint angle tracking.

The methods are evaluated based on two experiments. The first experiment, with a known sensor attachment as ground truth, compares a simple and a complex motion and is used to show that estimation over a short time window of just ten seconds of joint motion yields plausible and consistent joint axes. The second experiment, with OMC as ground truth, is used to validate that, while being much less restrictive, the proposed self-calibrating joint angle tracking provides the same accuracy as a conventional IMU-based approach.

2. Brief Review of the State of the Art in Anatomical Calibration

Anatomical calibration is the task of determining how the IMUs are attached to the body segments. In a broader sense, this also encompasses the pairing of IMUs to body segments [8,9] and the estimation of joint center positions [10–12]. The most relevant aspect, however, is to determine how the sensor coordinate system is rotated with respect to anatomical body segment axes (cf. Figure 1). In order to uniquely define this orientation, the coordinates of two anatomical axes need to be known in the sensor frame (or vice versa). Since errors in the sensor-to-segment orientations lead to kinematic cross-task and thus directly cause errors in the obtained joint angles [13–15], the reliability and accuracy of anatomical calibration methods are of fundamental interest in IMU-based motion analysis.

There are four main approaches for how to deal with the need for sensor-to-segment alignment in IMU-based human motion analysis [3]:

 doi:10.20944/preprints202211.0035.v1

1. relying on a precisely defined sensor attachment (*assumed alignment*),
2. calibration via measurements from additional devices (*augmented data*),
3. calibration based on precisely defined poses or motions (*functional alignment*),
4. calibration from arbitrary motions (*model-based alignment*).

Using a precisely defined attachment of the sensors to the body is a common approach and, according to the survey by Vitali and Perkins [3], used by 42 % of recent publications. The advantage of this approach is that it only requires minimum effort from the subject, i.e., no extra calibration movements are required, and that it is simple to implement. However, placing the sensors on the body so that predefined sensor axes correspond to functional joint axes is error-prone even for experienced medical personnel and even more so when patients themselves attach the sensors. In a study with three operators, Bouvier *et al.* [16] report reproducibility in the range of 4° to 12° and agreement with OMC in the range of 8° to 23°.

An example of an augmented data method for anatomical calibration is the use of an additional custom device equipped with an IMU that is used to determine the sensor orientation with respect to anatomical landmarks [17,18].

The third approach is to ask the subject to assume precisely defined postures or perform a sequence of precisely defined motions. In the simplest form, this consists of a single pose calibration, often in the N-pose or T-pose [19–22], and requires magnetometers in order to be able to define two axes from one pose. A magnetometer-free alternative is to use two poses, e.g., one standing up and one lying down [23], or to derive the anatomical axes from angular rate measurements of precisely defined motions, typically around the functional axes of the joint [24–26]. Often, both approaches are combined, and one axis is derived from a static pose and one from a functional motion. Those hybrid approaches have been demonstrated for the upper body [27,28] and lower body [29–31]. For thorax and lumbar joint angles, however, a recent study by Cottam *et al.* [32] found that calibration via functional motions did not improve accuracy in comparison to relying on manual sensor placement. Bouvier *et al.* [16] observe similar accuracy for precise attachment and for various calibration approaches based on precise poses and motions and point out that accuracy depends more on the rigor of the experimental procedure and operator training than on the calibration method. Furthermore, performing those motions can be tedious for the subject, especially considering that a precise execution is required. For patients with motor disabilities, performing precise motions can be hard or impossible. Even after solving those obstacles, the main drawback of those methods is that the accuracy of the calibration depends on the accuracy of performing the motion. An elegant recent approach is to use the actual motions of interest for calibration, e.g., during cycling [33] or walking [34]. However, this is only feasible in a limited amount of applications and relies on strong assumptions on the analyzed motions.

In many cases, e.g., clinical applications, it would render the use of IMUs much more practical if both a precisely known attachment and precisely specified calibration poses and motions could be avoided by determining the sensor-to-segment orientations from arbitrary motions, usually by relying on kinematic constraints of biomechanical models. This was demonstrated for the knee joint by exploiting a kinematic constraint in the angular rates of (approximate) hinge joints [4,10]. Furthermore, it was shown that extending this constraint for a combined optimization of a three-segment chain improves robustness [35] and that other methods, such as principal component analysis [36] and factor graph optimization [37,38], can be used to exploit hinge joint constraints. In [5,39], the gyroscope-based hinge joint constraint introduced in [10] and an accelerometer-based constraint are combined with an elaborate sample selection strategy, and in [40], both constraints are analyzed for observability of the joint axis. Taetz *et al.* [41] introduce an approach based on sliding window weighted least squares optimization that uses hinge-joint and range-of-motion constraints and a body-shape prior to simultaneously estimate the sensor-to-segment orientation along with the body motion. Zimmermann *et al.* [9] demonstrate that deep

Preprints (www.preprints.org) | NOT PEER-REVIEWED | Posted: 2 November 2022 doi:10.20944/preprints202211.0035.v1

learning can be used for lower body anatomical calibration with just two seconds of walking data.

For anatomical calibration based on arbitrary motions of 2-DoF joints, the existing work is limited. Müller *et al.* [6] introduce a gyroscope-based kinematic constraint for 2-DoF joints such as the elbow. Norden *et al.* [42] demonstrate that the same constraint can be employed for real-time estimation of hip and knee joint axes. However, the constraint used in both [6] and [42] assumes knowledge of the relative sensor orientation and therefore requires magnetometers. This poses a severe limitation for the applicability of those methods in indoor environments [43] and implies that temporary magnetic disturbances during calibration can lead to wrong axis estimates and thus permanently deteriorate the accuracy of the obtained joint angles. In [7], we presented first results of a magnetometer-free method that overcomes those restrictions by simultaneously estimating the heading offset.

3. Kinematic Model of 2-DoF Joints

The methods proposed in the present contribution perform automatic anatomical calibration for joints with two degrees of freedom (DoF). Those methods are suitable for any 2-DoF joint and can be applied to a range of biomechanical or robotic 2-DoF joints. To improve comprehensibility, the following description of the kinematic model and the calibration method focuses on the human elbow joint as an exemplary joint, which is later also used in the experimental evaluation.

Furthermore, even though in the following we always only consider two body segments connected by a single joint, the proposed methods can be used to analzye longer kinematic chains consisting of multiple segments. In this case, the calibration methods can be applied to each pair of segments that are connected by a 2-DoF joint.

Figure 2 shows an anatomical model of the combined elbow and radioulnar joint as an exemplary biological 2-DoF joint. The combined joint can perform two functional motions. Flexion and extension (FE) is performed by the elbow joint, while pronation and supination (PS) are the result of the radius pivoting around the ulna.

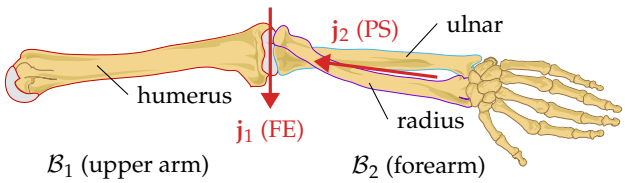

Figure 2. Anatomical model of the elbow joint and the radioulnar joint. The elbow joint is a hinge joint with the rotation axes $\mathbf{j}_1$, allowing for flexion and extension (FE). The radioulnar joint also has one degree of freedom ($\mathbf{j}_2$) and allows for pronation and supination (PS). For simplicity, we often refer to the combined radioulnar and elbow joint with two degrees of freedom as *elbow joint*.

As an approximation, we can model this joint – as well as any other 2-DoF joint – as a kinematic chain consisting of two hinge joints and one fixed rotation in between, as depicted in Figure 3. Including the fixed rotation, the sequence of rotations consists of flexion and extension (FE), a fixed carrying angle [44], and pronation and supination (PS).

We use unit quaternions to denote rotations and orientations [45]. In the context of quaternion multiplication, which we denote by $\otimes$, we implicitly regard 3D vectors as pure quaternions. Square brackets specify the coordinate system in which a vector is expressed, for example, $[\boldsymbol{\omega}_1]_{\mathcal{E}}$ is the gyroscope measurement of IMU $\mathcal{S}_1$ transformed into frame $\mathcal{E}$, i.e., $[\boldsymbol{\omega}_1]_{\mathcal{E}} = {}^{\mathcal{S}}_{\mathcal{E}}\mathbf{q} \otimes \boldsymbol{\omega}_1 \otimes {}^{\mathcal{S}}_{\mathcal{E}}\mathbf{q}^{-1}$. Here, the left upper and lower indices denote the frames between which the quaternion rotates. Quaternions that represent the rotation of an angle $\alpha \in \mathbb{R}$ around the axis $\mathbf{v} \in \mathbb{R}^3$ are written as $(\alpha \mathbin{@} \mathbf{v}) := \left[\cos\frac{\alpha}{2} \quad \frac{\mathbf{v}^\mathsf{T}}{\|\mathbf{v}\|}\sin\frac{\alpha}{2}\right]^\mathsf{T}$.

Preprints (www.preprints.org) | NOT PEER-REVIEWED | Posted: 2 November 2022 doi:10.20944/preprints202211.0035.v1

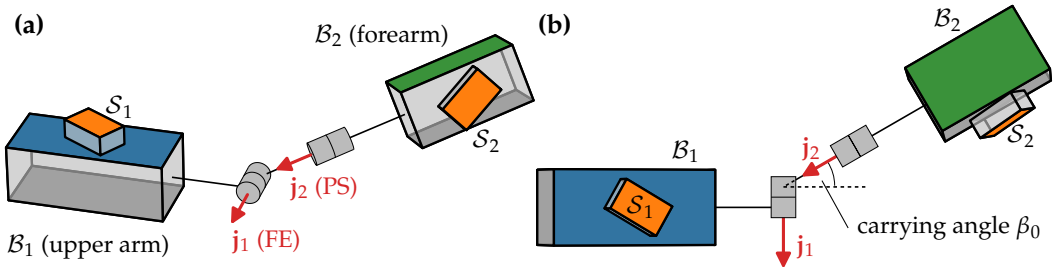

Figure 3. (a) Geometric kinematic model of the elbow joint. Inertial sensors $\mathcal{S}_1$ and $\mathcal{S}_2$ are placed in arbitrary orientation on the upper arm $\mathcal{B}_1$ and forearm $\mathcal{B}_2$. Upper arm and forearm are connected by two hinge joints that allow for FE ($\mathbf{j}_1$) and PS ($\mathbf{j}_2$). **(b)** View onto the $\mathbf{j}_1$-$\mathbf{j}_2$ plane. The fixed rotation between FE and PS is called *carrying angle*.

We can use this notation to mathematically express the orientation of the forearm $\mathcal{B}_2$ relative to the upper arm $\mathcal{B}_1$ using the FE joint angle $\alpha(t)$, the carrying angle β_0, and the PS angle $\gamma(t)$ as

$$ {}^{\mathcal{B}_2}_{\mathcal{B}_1}\mathbf{q} = (\alpha(t) \mathbin{@} \mathbf{j}_1) \otimes (\beta_0 \mathbin{@} \mathbf{j}_1 \times \mathbf{j}_2) \otimes (\gamma(t) \mathbin{@} \mathbf{j}_2). \tag{1} $$

The International Society of Biomechanics (ISB) [44] also recommends this joint model for the elbow and precisely defines coordinate systems $\mathcal{B}_1$ and $\mathcal{B}_2$ so that $[\mathbf{j}_1]_{\mathcal{B}1} = [0\ 0\ 1]^\intercal$ and $[\mathbf{j}_2]_{\mathcal{B}2} = [0\ 1\ 0]^\intercal$. When using this definition, the joint angles are intrinsic z-x'-y'' Euler angles of ${}^{\mathcal{B}_2}_{\mathcal{B}_1}\mathbf{q}$. Please note that this also means that the axis $\mathbf{j}_1$ (FE) is fixed in the coordinate system of a sensor attached to the upper arm, while the axis $\mathbf{j}_2$ (PS) is fixed in the coordinate system of a sensor attached to the forearm.

Instead of using regular Euler angles, we could consider modeling a 2-DoF joint with axes that are all potentially non-orthogonal (including the carrying angle axis). However, as Appendix A shows, any generic model with non-orthogonal axes can also be expressed using standard z-x'-y'' Euler angles by redefining the segment coordinate systems accordingly. This means that the choice of z-x'-y'' Euler angles according to the ISB recommendations [44] does not restrict the generality of the proposed methods. Also, note that the orientation of the IMUs on the body segments is independent of this definition. The goal of anatomical calibration is to determine the fixed coordinates $\mathbf{j}_1$ and $\mathbf{j}_2$ of the functional joint axes in the local coordinate systems of the respective IMUs.

4. Proposed Methods

Two IMUs $\mathcal{S}_1$ and $\mathcal{S}_2$ are placed on the subject in unknown orientations, one on each body segment connected by the 2-DoF joint (i.e., in case of the elbow, one on the upper arm and one on the forearm). Assume that we can estimate the sensor orientation quaternions ${}^{\mathcal{S}_1}_{\mathcal{E}}\mathbf{q}(t_k)$, ${}^{\mathcal{S}_2}_{\mathcal{E}}\mathbf{q}(t_k)$ relative to a common inertial frame $\mathcal{E}$. We also measure the angular rates $\boldsymbol{\omega}_1(t_k) \in \mathbb{R}^3$, $\boldsymbol{\omega}_2(t_k) \in \mathbb{R}^3$ of the IMUs, in their respective local coordinate systems. All measurements are sampled at times $t_k = kT_\mathrm{s}, k \in \{1, 2, \ldots, N\}, T_\mathrm{s} \in \mathbb{R}_{>0}$. Note that the assumption of a common inertial frame $\mathcal{E}$ is restrictive in practice as it assumes 9D sensor fusion in a perfectly homogeneous magnetic field and will later be dropped.

In the following, we will derive two different kinematic constraints for 2-DoF joints, one based on the angular rate and one based on the segment orientations, that are both suitable for 6D sensor fusion with unknown heading offset. Based on those constraints, we introduce methods for automatic anatomical calibration and for magnetometer-free joint angle calculation.

4.1. Rotation-Based Kinematic Joint Constraint

As shown in Section 3, a 2-DoF joint cannot perform arbitrary joint rotation in all directions. Instead, rotation is only possible around the two joint axes. In the following, we will investigate how this translates to a kinematic constraint in the angular rates measured

Preprints (www.preprints.org) | NOT PEER-REVIEWED | Posted: 2 November 2022 doi:10.20944/preprints202211.0035.v1

by the two IMUs. We will later exploit this constraint to estimate joint axes from arbitrary joint motion.

Using the addition theorem for angular velocities, we express the relationship between the gyroscope measurements $\boldsymbol{\omega}_1(t_k)$ and $\boldsymbol{\omega}_2(t_k)$ as

$$[\boldsymbol{\omega}_2]_\mathcal{E} = [\boldsymbol{\omega}_1]_\mathcal{E} + \omega_{j_1}[\mathbf{j}_1]_\mathcal{E} + \omega_{j_2}[\mathbf{j}_2]_\mathcal{E}. \tag{2}$$

The scalars ω_{j_1} and ω_{j_2} are the rotation rates of the joint around the respective joint axes. In case of joints with two degrees of freedom according to the model in Figure 3, this corresponds to the anatomical joint motions, i.e., in case of the elbow, ω_{j_1} is the FE angular rate and ω_{j_2} the PS angular rate. This means that the angular rate $\boldsymbol{\omega}_2$ measured by the forearm IMU $\mathcal{S}_2$ is composed of three components:

1. the common rotation of the whole arm, also observed by IMU $\mathcal{S}_1$ as $\boldsymbol{\omega}_1$
2. the FE rotation around $\mathbf{j}_1$
3. the PS rotation around $\mathbf{j}_2$.

Note that the carrying angle does not appear, since it is time-invariant. Also note that in (2), the angular rates and joint axes are transformed into a common coordinate system, here $\mathcal{E}$.

For hinge joints, in [4], the following constraint has been derived from (2):

$$\|\boldsymbol{\omega}_1 \times \mathbf{j}_1\| - \|\boldsymbol{\omega}_2 \times \mathbf{j}_2\| = 0. \tag{3}$$

Since this version of the constraint only uses quantities given in local sensor coordinates, it is independent of sensor orientations with respect to a fixed frame and thus not affected by magnetic disturbances.

For joints with two degrees of freedom, we need to know the relative sensor orientation or sensor orientations with respect to a common fixed frame. In order to derive a similar constraint from (2) for 2-DoF joints, we calculate the scalar product with the normalized[1] axis $[\mathbf{j}_1]_\mathcal{E} \times [\mathbf{j}_2]_\mathcal{E}$ on both sides, i.e.,

$$\left([\boldsymbol{\omega}_2]_\mathcal{E} - \omega_{j_2}[\mathbf{j}_2]_\mathcal{E}\right) \cdot \frac{[\mathbf{j}_1]_\mathcal{E} \times [\mathbf{j}_2]_\mathcal{E}}{\|[\mathbf{j}_1]_\mathcal{E} \times [\mathbf{j}_2]_\mathcal{E}\|} = \left([\boldsymbol{\omega}_1]_\mathcal{E} + \omega_{j_1}[\mathbf{j}_1]_\mathcal{E}\right) \cdot \frac{[\mathbf{j}_1]_\mathcal{E} \times [\mathbf{j}_2]_\mathcal{E}}{\|[\mathbf{j}_1]_\mathcal{E} \times [\mathbf{j}_2]_\mathcal{E}\|}, \tag{4}$$

and employ the fact that $\mathbf{a} \cdot (\mathbf{a} \times \mathbf{b}) = \mathbf{a} \cdot (\mathbf{b} \times \mathbf{a}) = 0$. This yields

$$\left([\boldsymbol{\omega}_1]_\mathcal{E} - [\boldsymbol{\omega}_2]_\mathcal{E}\right) \cdot \frac{[\mathbf{j}_1]_\mathcal{E} \times [\mathbf{j}_2]_\mathcal{E}}{\|[\mathbf{j}_1]_\mathcal{E} \times [\mathbf{j}_2]_\mathcal{E}\|} = 0. \tag{5}$$

For perfect 2-DoF joints and ideal IMU measurements, this constraint must be fulfilled for each sampling instant. For biological joints, and when taking soft tissue motion and measurement errors into account, the constraint is still valid in a least-squares sense when considering a short motion sequence consisting of multiple samples.

However, the constraint as formulated in (5) uses the reference frame $\mathcal{E}$ and is only suitable for use in combination with 9D inertial orientation estimation (IOE), i.e., with the use of magnetometers. Since magnetic fields are often severely disturbed [43], we want to avoid using magnetometer measurements and therefore only employ 6D sensor fusion to estimate the sensor orientations, e.g., using the VQF algorithm [47]. This implies that the heading of the estimated orientations is not well-defined. More precisely, this can be described by the estimated orientations ${}^{\mathcal{S}_1}_{\mathcal{E}_1}\mathbf{q}$ and ${}^{\mathcal{S}_2}_{\mathcal{E}_2}\mathbf{q}$ being given in different global reference frames $\mathcal{E}_1$ and $\mathcal{E}_2$, which are rotated around the vertical global z-axis, i.e.,

$${}^{\mathcal{E}_2}_{\mathcal{E}_1}\mathbf{q} = (\delta(t) \mathbin{@} [0 \;\; 0 \;\; 1]^\mathsf{T}) = \left[\cos\left(\tfrac{\delta(t)}{2}\right) \quad 0 \quad 0 \quad \sin\left(\tfrac{\delta(t)}{2}\right)\right]^\mathsf{T}. \tag{6}$$

[1] Normalizing the axis was found to improve robustness compared to the constraint presented in [46].

Preprints (www.preprints.org) | NOT PEER-REVIEWED | Posted: 2 November 2022 doi:10.20944/preprints202211.0035.v1

The heading offset $\delta(t)$ has an unknown initial value and then slowly drifts due to gyroscope bias [48]. Please note that both $\mathcal{E}_1$ and $\mathcal{E}_2$ have some unknown heading offset with respect to a fixed frame $\mathcal{E}$ used in 9D sensor fusion and defined by gravity and the Earth's magnetic field. However, knowing those individual offsets is not necessary for calculating relative orientations and joint angles.

We take the heading offset into account by evaluating the constraint (5) in one of the slowly-drifting global frames (here $\mathcal{E}_1$), i.e.,

$$\underbrace{\left([\boldsymbol{\omega}_1]_{\mathcal{E}_1} - [\boldsymbol{\omega}_2]_{\mathcal{E}_1}\right)}_{=:\boldsymbol{\omega}_{\text{rel}}} \cdot \underbrace{\frac{[\mathbf{j}_1]_{\mathcal{E}_1} \times [\mathbf{j}_2]_{\mathcal{E}_1}}{\left\| [\mathbf{j}_1]_{\mathcal{E}_1} \times [\mathbf{j}_2]_{\mathcal{E}_1} \right\|}}_{=:\mathbf{j}_n/\|\mathbf{j}_n\|} = 0. \tag{7}$$

This version of the constraint implicitly depends on δ, as we need the quaternion ${}^{\mathcal{S}_2}_{\mathcal{E}_1}\mathbf{q} = {}^{\mathcal{E}_2}_{\mathcal{E}_1}\mathbf{q}(\delta) \otimes {}^{\mathcal{S}_2}_{\mathcal{E}_2}\mathbf{q}$ to transform $\boldsymbol{\omega}_2$ and $\mathbf{j}_2$ to $\mathcal{E}_1$ coordinates. This means that instead of (5) we can use (7) with magnetometer-free 6D orientations and that, in addition to the joint axes coordinates, we also identify the current heading offset $\delta(t)$ as an additional parameter.

4.2. Orientation-Based Kinematic Joint Constraint

As an alternative, we derive a second kinematic joint constraint. In contrast to the constraint introduced in the previous section, this constraint is not based on the joint rotation but on the joint orientation, i.e., the relative orientation between the two body segments connected by the joint.

As in Section 4.1, assume that we have 6D sensor orientation estimates ${}^{\mathcal{S}_1}_{\mathcal{E}_1}\mathbf{q}(t_k)$, ${}^{\mathcal{S}_2}_{\mathcal{E}_1}\mathbf{q}(t_k)$, e.g., estimated with the VQF algorithm [47]. As before, our aim is to identify $[\mathbf{j}_1]_{\mathcal{S}_1}$, $[\mathbf{j}_2]_{\mathcal{S}_2}$, and the heading offset $\delta(t)$. For any given estimate of those values, we are able to calculate joint angles. If the joint follows the 2-DoF joint model introduced in Section 3, the following statement holds true: With the correct sensor-to-segment orientation and the correct heading offset, the second joint angle (for the elbow joint: the carrying angle) is constant.

Mathematically, we can formulate this by calculating the joint orientation and then decomposing this orientation into Euler angles. First, we determine the shortest-possible rotations that align the estimated sensor axes with the joint axes:

$${}^{\mathcal{B}_1}_{\mathcal{S}_1}\mathbf{q} = \left(\arccos\left([0\ 0\ 1]^\intercal \cdot [\mathbf{j}_1]_{\mathcal{S}_1}\right) @ [0\ 0\ 1]^\intercal \times [\mathbf{j}_1]_{\mathcal{S}_1}\right) \tag{8}$$

$${}^{\mathcal{B}_2}_{\mathcal{S}_2}\mathbf{q} = \left(\arccos\left([0\ 1\ 0]^\intercal \cdot [\mathbf{j}_2]_{\mathcal{S}_2}\right) @ [0\ 1\ 0]^\intercal \times [\mathbf{j}_2]_{\mathcal{S}_2}\right) \tag{9}$$

and calculate the rotation quaternion between the reference frames

$${}^{\mathcal{E}_2}_{\mathcal{E}_1}\mathbf{q} = (\delta @ [0\ 0\ 1]^\intercal). \tag{10}$$

Using those quaternions we calculate the joint orientation

$${}^{\mathcal{B}_2}_{\mathcal{B}_1}\mathbf{q} = {}^{\mathcal{S}_1}_{\mathcal{B}_1}\mathbf{q} \otimes \underbrace{{}^{\mathcal{E}_1}_{\mathcal{S}_1}\mathbf{q} \otimes {}^{\mathcal{E}_2}_{\mathcal{E}_1}\mathbf{q} \otimes {}^{\mathcal{S}_2}_{\mathcal{E}_2}\mathbf{q}}_{={}^{\mathcal{S}_2}_{\mathcal{S}_1}\mathbf{q}} \otimes {}^{\mathcal{B}_2}_{\mathcal{S}_2}\mathbf{q}, \tag{11}$$

which depends on the sensor orientations, the estimated joint axes $\mathbf{j}_1$ and $\mathbf{j}_2$, and the heading offset δ.

Preprints (www.preprints.org) | NOT PEER-REVIEWED | Posted: 2 November 2022 doi:10.20944/preprints202211.0035.v1

Therefore, ${}^{\mathcal{B}_2}_{\mathcal{B}_1}\mathbf{q} =: [\, q_w \;\; q_x \;\; q_y \;\; q_z \,]^\intercal$ can be calculated from the measured data and the estimated parameters. The second intrinsic z-x'-y'' Euler angle of this quaternion, i.e., the estimated carrying angle, is

$$\hat{\beta}_0 = \arcsin\left(2q_w q_x + 2q_y q_z\right). \tag{12}$$

Due to the joint constraint, this angle has to be constant over the whole measurement window, i.e., with the fixed constant carrying angle β_0,

$$\arcsin\left(2q_w q_x + 2q_y q_z\right) = \beta_0. \tag{13}$$

Similar to (7), the constraint (13) can be used to identify the joint axes coordinates and the heading offset δ. Additionally, unless the actual value of the carrying angle β_0 is known, β_0 has to be identified as an additional parameter.

4.3. Parametrization of Joint Axes

The aim of the anatomical calibration is to identify the joint axes $\mathbf{j}_1 \in \mathbb{R}^3$ and $\mathbf{j}_2 \in \mathbb{R}^3$ with $\|\mathbf{j}_i\| = 1$, $i = 1, 2$. Parametrizing the axes as Cartesian vectors in an optimization problem is inconvenient as we would need an additional constraint to ensure unit length. Therefore, we employ spherical coordinates and represent each axis by two parameters φ_i and θ_i, e.g.,

$$\mathbf{j}_i = [\, \sin\theta_i \cos\varphi_i \;\; \sin\theta_i \sin\varphi_i \;\; \cos\theta_i \,]^\intercal, \quad i = 1, 2. \tag{14}$$

With the parametrization given in (14), $\frac{\partial \mathbf{j}_i}{\partial \varphi_i} = 0$ if $\sin\theta_i = 0$. To avoid this singularity, we introduce an alternative spherical representation of the same joint axis direction, as shown in Figure 4. During optimization, we always use a parametrization with $|\sin\theta_i| \gg 0$ by converting the axis to Cartesian coordinates and then to the other representation whenever the current representation comes close ($< 30°$) to that singularity.

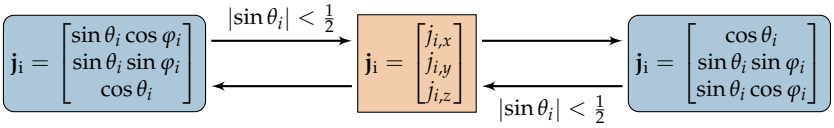

Figure 4. Two spherical parametrizations are used to represent the joint axes $\mathbf{j}_i$, $i = 1, 2$, with two parameters each, θ_i and φ_i. To avoid the derivative becoming close to zero, we convert the respective axis to Cartesian coordinates and then to the other representation whenever $|\sin\theta_i| < 0.5$.

This approach ensures that the derivatives with respect to the joint axes are always sufficiently sensitive.

4.4. Cost Function and Optimization

Sample selection is performed to fill a sample buffer of M data sets

$$\left\{ {}^{\mathcal{S}_1}_{\mathcal{E}_1}\mathbf{q}(t_k), {}^{\mathcal{S}_2}_{\mathcal{E}_2}\mathbf{q}(t_k), [\boldsymbol{\omega}_1]_{\mathcal{E}_1}(t_k), [\boldsymbol{\omega}_2]_{\mathcal{E}_2}(t_k) \right\} \tag{15}$$

for the rotation-based constraint and

$$\left\{ {}^{\mathcal{S}_1}_{\mathcal{E}_1}\mathbf{q}(t_k), {}^{\mathcal{S}_2}_{\mathcal{E}_2}\mathbf{q}(t_k) \right\} \tag{16}$$

for the orientation-based constraint from the 6D orientation quaternions and angular rates measured at a (potentially very high) sampling frequency of f_s. The proposed method employs a regular (equidistant) sample selection strategy that stores one sample every 0.05 s. Note that this method can easily be extended by more sophisticated sample selection strategies since the optimization procedure does not require equidistant sampling.

Preprints (www.preprints.org) | NOT PEER-REVIEWED | Posted: 2 November 2022 doi:10.20944/preprints202211.0035.v1

In order to determine the joint axes and heading offset that best satisfy the rotation-based constraint (7) in a least-squares sense, we define the error for each sampling instant t_k as

$$e(t_k) := \boldsymbol{\omega}_{\mathrm{rel}}(\delta) \cdot \frac{\mathbf{j}_{\mathrm{n}}(\boldsymbol{\Phi})}{\|\mathbf{j}_{\mathrm{n}}(\boldsymbol{\Phi})\|}, \tag{17}$$

with the parameter vector $\boldsymbol{\Phi} := [\,\theta_1 \;\; \varphi_1 \;\; \theta_2 \;\; \varphi_2 \;\; \delta\,]^\intercal$. Note that we assume the heading offset $\delta(t)$ to be constant for all samples in the current buffer, which is valid for short window lengths.

Similarly, for the orientation-based constraint (13), we define the error as

$$e(\boldsymbol{\Phi}) := \arcsin\left(2q_w q_x + 2q_y q_z\right) - \beta_0, \tag{18}$$

with a parameter vector $\boldsymbol{\Phi} := [\,\theta_1 \;\; \varphi_1 \;\; \theta_2 \;\; \varphi_2 \;\; \delta \;\; \beta_0\,]^\intercal$ that additionally includes the carrying angle.

To estimate the joint axes $\mathbf{j}_1$ and $\mathbf{j}_2$ and the heading offset δ given a set of M samples, we find the parameter vector $\hat{\boldsymbol{\Phi}}$ that minimizes the sum of squares of the error using the Gauss-Newton algorithm [49]. Appendix B gives details on the optimization algorithm, provides analytical expressions for the gradients of the cost function, and introduces a moving window approach for employing the proposed method in real-time applications. As a result of the optimization step, we obtain the joint axes $\mathbf{j}_1$ and $\mathbf{j}_2$ in the coordinates systems of sensors $\mathcal{S}_1$ and $\mathcal{S}_2$, respectively, and the heading offset δ between the reference frames $\mathcal{E}_1$ and $\mathcal{E}_2$.

4.5. Joint Angle Calculation

Using the optimization results, we calculate FE and PS joint angles based on the ISB recommendations [44]. Those joint angles are defined as intrinsic z-x'-y'' Euler angles of the forearm $\mathcal{B}_2$ relative to the upper arm $\mathcal{B}_1$, i.e., ${}^{\mathcal{B}_2}_{\mathcal{B}_1}\mathbf{q}$, with $\mathcal{B}_1$ and $\mathcal{B}_2$ being the segment coordinate systems as defined in [44].

From 6D IOE, we get the sensor orientation quaternions ${}^{\mathcal{S}_1}_{\mathcal{E}_1}\mathbf{q}$ and ${}^{\mathcal{S}_2}_{\mathcal{E}_2}\mathbf{q}$. After performing the optimization, we know the coordinates of both joint axes $\mathbf{j}_1$ and $\mathbf{j}_2$ in local sensor coordinates and the heading offset δ. Note that additional knowledge is needed to determine the absolute value of the joint angles without any offset – for example, for the elbow joint, which joint orientation corresponds to zero flexion and zero pronation is only a matter of convention and not an inherent property of the 2-DoF joint. To obtain offset-free angles, we employ reference values of the FE and PS joint angles at one arbitrary time instant t_{ref}, e.g., obtained from a known pose or by exploiting the maximum range of motion of the joint. With those values, the joint angles can be calculated by the algorithm described below:

First, we calculate ${}^{\mathcal{E}_2}_{\mathcal{E}_1}\mathbf{q}$ via (6) and use this to obtain ${}^{\mathcal{S}_2}_{\mathcal{S}_1}\mathbf{q} = {}^{\mathcal{E}_2}_{\mathcal{E}_1}\mathbf{q} \otimes {}^{\mathcal{S}_2}_{\mathcal{E}_2}\mathbf{q}$. Then we determine rotations that ensure that the identified joint axes match the joint axes defined in [44]:

$${}^{\mathcal{B}'_1}_{\mathcal{S}_1}\mathbf{q} = \left(\arccos([0\;0\;1]^\intercal \cdot \mathbf{j}_1)\,@\,[0\;0\;1]^\intercal \times \mathbf{j}_1\right) \tag{19}$$

$${}^{\mathcal{B}'_2}_{\mathcal{S}_2}\mathbf{q} = \left(\arccos([0\;1\;0]^\intercal \cdot \mathbf{j}_2)\,@\,[0\;1\;0]^\intercal \times \mathbf{j}_2\right). \tag{20}$$

Using those, we calculate the relative segment orientation

$${}^{\mathcal{B}'_2}_{\mathcal{B}'_1}\mathbf{q} = \left({}^{\mathcal{S}_1}_{\mathcal{E}_1}\mathbf{q} \otimes {}^{\mathcal{B}'_1}_{\mathcal{S}_1}\mathbf{q}\right)^{-1} \otimes {}^{\mathcal{S}_2}_{\mathcal{E}_1}\mathbf{q} \otimes {}^{\mathcal{B}'_2}_{\mathcal{S}_2}\mathbf{q}. \tag{21}$$

Preprints (www.preprints.org) | NOT PEER-REVIEWED | Posted: 2 November 2022 doi:10.20944/preprints202211.0035.v1

For any quaternion $\mathbf{q} =: [\, q_w \;\; q_x \;\; q_y \;\; q_z \,]^\mathsf{T}$, the z-x'-y'' Euler angles (α, β, γ) can be calculated as

$$\alpha = \operatorname{atan2}(2q_w q_z - 2q_x q_y, q_w^2 - q_x^2 + q_y^2 - q_z^2), \tag{22}$$
$$\beta = \arcsin(2q_w q_x + 2q_y q_3), \tag{23}$$
$$\gamma = \operatorname{atan2}(2q_w q_y - 2q_x q_z, q_w^2 - q_x^2 - q_y^2 + q_z^2). \tag{24}$$

By calculating z-x'-y'' Euler angles $(\alpha', \beta', \gamma')$ of ${}^{\mathcal{B}_2'}_{\mathcal{B}_1'}\mathbf{q}$, we obtain the FE angle α' and the PS angle γ' that only differ from the well-defined joint angles according to [44] by a constant offset that depends on the actual placement of the IMUs.

We can eliminate this offset by exploiting knowledge of the actual joint angles α_{ref} and γ_{ref} at $t = t_{\text{ref}}$. The segment-to-sensor orientations

$${}^{\mathcal{B}_1}_{\mathcal{S}_1}\mathbf{q} = {}^{\mathcal{B}_1'}_{\mathcal{S}_1}\mathbf{q} \otimes \left(\alpha'(t_{\text{ref}}) - \alpha_{\text{ref}} \,@\, [0\ 0\ 1]^\mathsf{T}\right), \tag{25}$$
$${}^{\mathcal{B}_2}_{\mathcal{S}_2}\mathbf{q} = {}^{\mathcal{B}_2'}_{\mathcal{S}_2}\mathbf{q} \otimes \left(\gamma_{\text{ref}} - \gamma'(t_{\text{ref}}) \,@\, [0\ 1\ 0]^\mathsf{T}\right) \tag{26}$$

allow us to calculate ${}^{\mathcal{B}_2}_{\mathcal{B}_1}\mathbf{q} = ({}^{\mathcal{S}_1}_{\mathcal{E}_1}\mathbf{q} \otimes {}^{\mathcal{B}_1}_{\mathcal{S}_1}\mathbf{q})^{-1} \otimes {}^{\mathcal{S}_2}_{\mathcal{E}_1}\mathbf{q} \otimes {}^{\mathcal{B}_2}_{\mathcal{S}_2}\mathbf{q}$. The Euler angles $(\alpha, \beta_0, \gamma)$ of ${}^{\mathcal{B}_2}_{\mathcal{B}_1}\mathbf{q}$ are the offset-free FE and PS joint angles α and γ, respectively, and the carrying angle β_0 (cf. Figure 3), which is almost constant and rarely reported [44].

To further improve the proposed method, in Appendix C, we introduce an optional extension that allows for the rotation-based constraint to be used when only orientation data is available (e.g., if on-chip sensor fusion is used), add a low-pass filter to reduce the influence of soft tissue motion artifacts, and discuss options for how to resolve the ambiguity in the signs of the joint axes.

5. Experimental Evaluation

We evaluate the proposed magnetometer-free anatomical calibration and joint angle calculation methods based on two experiments.

The first experiment is designed to evaluate if the obtained joint axis estimates are plausible and consistent. To this end, IMU data from two different motions is recorded from five subjects and a mechanical joint, while carefully attaching the sensors in a known orientation. Each trial is split into overlapping time windows to which the anatomical calibration methods are applied. The obtained joint axis estimates are compared to the axes obtained by the more restrictive method of careful manual sensor placement.

The second experiment is designed for the evaluation of the accuracy of the obtained joint angles with the proposed self-calibrating magnetometer-free joint angle calculation method. This experiment consists of recordings of natural everyday life motions of two subjects. It uses marker-based OMC as a reference, which allows for the comparison of the obtained joint angles to joint angles obtained from optical markers and from a conventional 9D IMU-based approach. As a further validation step, we consider the variability of the expected-to-be-constant carrying angle as a metric for how well the estimated joint axes describe the functional joint motion.

Note that in all experiments, the sensors are carefully attached in a known orientation to facilitate a plausibility check of the obtained results. To still verify that the proposed methods do not make assumptions regarding the sensor orientation, we simulate a random sensor attachment by multiplying all gyroscope and accelerometer measurements with a random rotation matrix that is different for each time window.

The extension for on-chip sensor fusion introduced in Section C.1 is always used, i.e., the angular rates used for evaluating the rotation-based kinematic constraint are derived from the orientation estimates. Since the impact on the results is negligible, the results obtained using the actual gyroscope measurements are not shown separately.

Preprints (www.preprints.org) | NOT PEER-REVIEWED | Posted: 2 November 2022 doi:10.20944/preprints202211.0035.v1

5.1. Robustness of Joint Axis Estimation

The first experiment is performed to answer the following two research questions:

1. Are the estimated joint axes plausible, i.e., do they agree with the values expected based on careful manual placement?
2. Are the estimated joint axes consistent, i.e., do we always obtain the same result when using different parts of the trial?

Data from five healthy subjects is recorded. Inertial sensors (Xsens MTw, Xsens Technologies B.V., Netherlands) are placed on the upper arm close to the elbow and on the forearm close to the wrist. The sensors are placed in a defined orientation on the skin so that one local sensor axis coincides roughly with the functional joint axis.

We define two different motions:

1. The *simple motion* consists of FE of the elbow and PS of the forearm, performed alternatingly while keeping the arm in the frontal plane of the shoulder.
2. For the *complex motion*, we ask the subject to perform random combinations of FE and PS, allowing for 3D rotation of the shoulder including humeral rotation.

Each subject performs both motions for approximately one minute.

In addition to the five human subjects, an additional data set is recorded using a mechanical joint. This joint has dimensions similar to the human arm and consists of two hinge joints as shown in Figure 3. During the recordings, the joint was held in hand and moved in a way that mimics the motions performed by the five subjects.

For each recording, the proposed methods are used on 21 partially overlapping moving windows w, $w = 1, 2, \ldots, 21$, of length 10 s with data sets recorded every 0.05 s. Note that we will later investigate the effect of window length and sampling time and show that this window length is usually sufficient to identify the joint axes and that collecting data sets more frequently does not significantly improve the robustness.

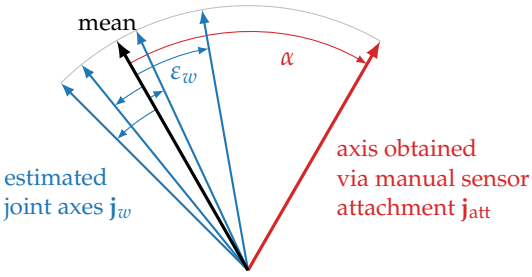

Figure 5. Variability angle ε_w and misalignment angle α used to evaluate the axis estimation results. ε_i is the angle between the estimated axis for a single window and the mean estimate. α is the angle between the mean estimate and the axis obtained by careful manual sensor attachment. For a good anatomical calibration method, ε_i should be small, showing that the estimates are consistent, and α should be within 30°, showing that the estimates are plausible.

Since the only available ground truth are approximate axis coordinates that we know due to the orientation in which the sensor was attached, we define suitable evaluation metrics that allow us to quantify the consistency and plausibility of the estimates. See Figure 5 for an illustration of the definitions. First, denote the estimated joint axes $\mathbf{j}_w$, with w being the index for the estimation window.[2] To assess if the estimates are consistent, we define the *variability angle*

$$\varepsilon_w = \sphericalangle(\mathbf{j}_w, \mathbf{j}_{\text{mean}}), \tag{27}$$

[2] For a compact notation, we now omit the segment index, denoting whether the axis is a FE axis or a PS axis.

Preprints (www.preprints.org) | NOT PEER-REVIEWED | Posted: 2 November 2022 doi:10.20944/preprints202211.0035.v1

where $\sphericalangle$ denotes the angle between two 3D vectors and

$$\mathbf{j}_{\text{mean}} = \frac{1}{21} \sum_{w=1}^{21} \mathbf{j}_w \tag{28}$$

is the mean of all estimates. In other words, ε_w is the angular deviation between the estimate for window w and the mean of all estimates. If this angle is always small, the estimation results agree well for all time windows.

To also check if this result is plausible, we introduce the *misalignment angle*

$$\alpha = \sphericalangle(\mathbf{j}_{\text{mean}}, \mathbf{j}_{\text{att}}), \tag{29}$$

with $\mathbf{j}_{\text{att}}$ being the joint axis obtained via careful manual sensor attachment. Therefore, α is the angle between the mean estimation result and the axis obtained via manual sensor attachment. While precise manual sensor attachment is hard and error-prone, we can at least expect both axes to coincide roughly and therefore consider the result plausible if $\alpha \leq 30°$.

Figure 6 shows the results obtained in the first experiment with the rotation-based and orientation-based constraints. In general, we see that the proposed methods for anatomical calibration produce good results: with both constraints, the methods are able to determine plausible FE and PS joint axes from 10-second recordings, and in all cases except for subject 2 with the orientation-based constraint and the complex motion, the median of the variability angle ε_w is below 10°. In other words, almost all time windows lead to axis estimates within the expected range. As a main result, it is noticeable that the rotation-based constraint performs better than the orientation-based constraint and that a slight increase in the variability angles ε_w can be observed in the complex motion. This is likely due to soft tissue motion caused by humeral rotation. Furthermore, the randomness of the complex motion can lead to longer periods of motion that do not excite both degrees of freedom of the joint.

The results obtained with the mechanical joint agree very well with the expected axes ($\alpha \leq 2°$), and the joint axis estimates are more consistent than for the biological elbow joints. This is to be expected since precisely attaching the sensors is easier with the mechanical joints, there are no soft tissue motion artifacts, and the mechanical joint constructed with two hinge joints follows the kinematic model (Figure 3) more precisely than the human elbow.

To facilitate an intuitive understanding of the results, Figure 7 shows the estimated and expected joint axes in a 3D visualization of the respective IMU coordinate systems. We can see that, for both FE and PS, the joint axis estimates of all overlapping time windows agree well. While the PS axis agrees very well with the axis expected due to sensor alignment, a systematic disagreement of $\sim$17° between the estimated and expected axes is noticeable. Since all estimates are very consistent, this is most likely due to an imprecise manual attachment of the sensor, causing the y-axis to disagree with the functional PS axis of the joint. In general, we see in Figure 6 that the misalignment angle α is larger for the FE axis $\mathbf{j}_1$ than for the PS axis $\mathbf{j}_2$. This is plausible, given the fact that the longitudinal x-axis of the IMU is much easier to precisely align with the longitudinal axis of the forearm, whereas aligning the y-axis of the upper arm IMU, corresponding to a much shorter dimension of the sensor case, with the functional FE axis was found to be much harder while conducting the experiments.

Preprints (www.preprints.org) | NOT PEER-REVIEWED | Posted: 2 November 2022 doi:10.20944/preprints202211.0035.v1

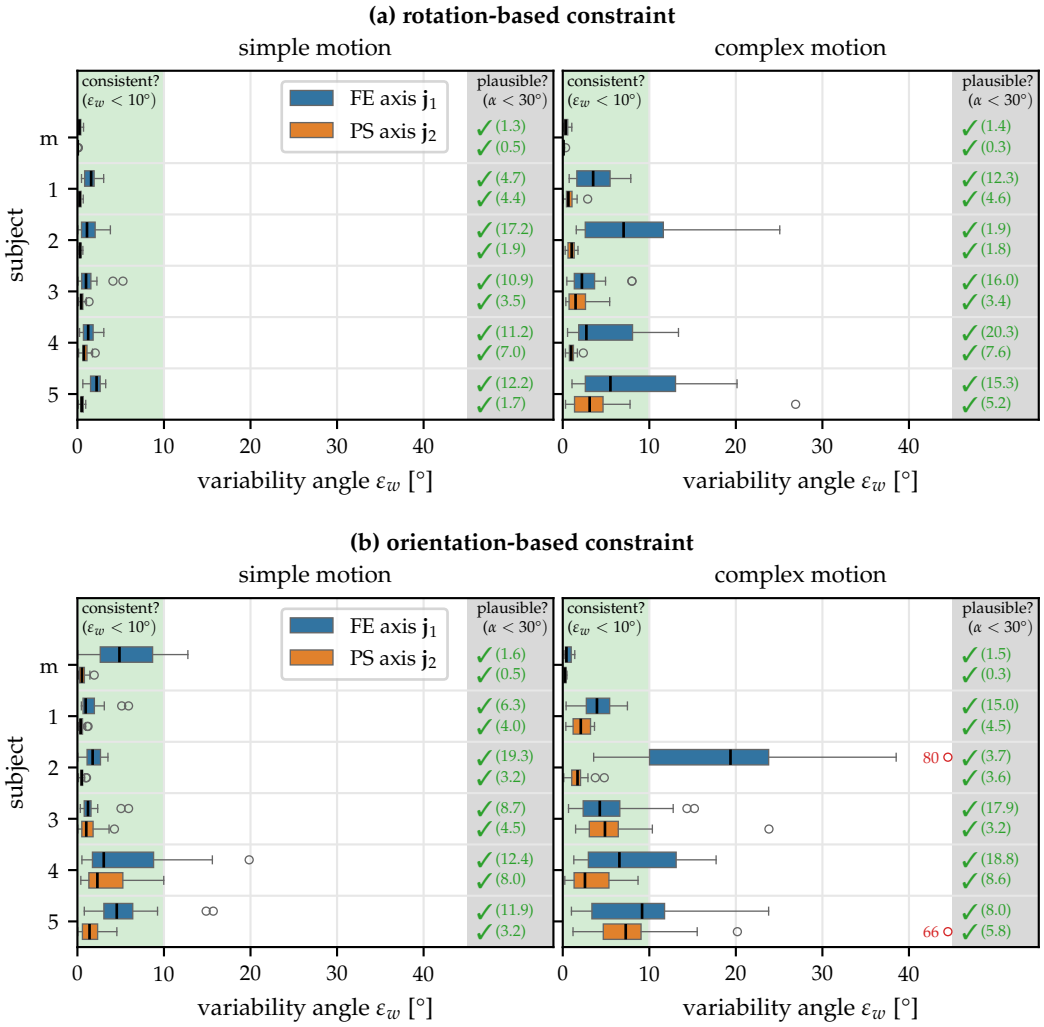

Figure 6. Consistency and plausibility results for the first experiment with the **(a)** rotation-based constraint and the **(b)** orientation-based constraint, for two motion types and for five human subjects and a mechanical joint (m). The proposed methods estimate plausible axes for all subjects and all motions. The rotation-based constraint yields more consistent estimates than the orientation-based constraint, and the simple motion leads to better results than the complex motion.

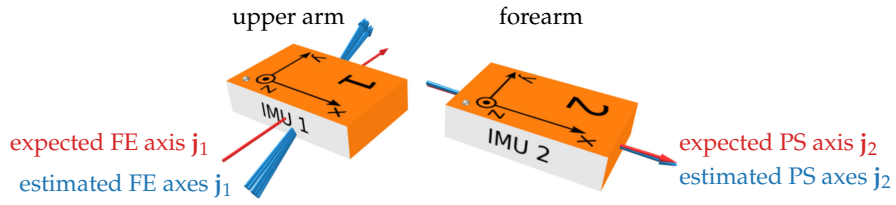

Figure 7. 3D visualization of the estimation results for an exemplary trial (subject 2, simple motion, rotation-based constraint). The joint axis estimates from all windows agree well (blue arrows). The PS axis agrees very well with the expected value (red arrow), while for the FE axis there is a misalignment of 17°, most likely due to imprecise manual sensor attachment.

However, it is noticeable that also for the variability angle ε_w, the values are typically much larger for the FE axis than for the PS axis, indicating that it is not only harder to perform a precise manual alignment of this axis but it is also harder for the proposed methods to accurately and consistently estimate this axis. This effect is especially pronounced for the complex motion.

Preprints (www.preprints.org) | NOT PEER-REVIEWED | Posted: 2 November 2022 doi:10.20944/preprints202211.0035.v1

To investigate one potential effect, we take a closer look at subject 2 and the rotation-based constraint. In the complex motion trials, subject 2 stands out as the range of motion of the upper arm IMU is significantly lower than for the other subjects (more specifically, the mean pairwise orientation difference within a window is 16° for subject 2 and between 46° and 56° for the other four subjects) while the FE axis deviations are larger than for all other subjects. In Figure 8, we visualize the estimated FE joint axes (Figure 8a) and notice that all estimates lie approximately within the y-z-plane of the sensor. During the trial, the x-axis of the upper arm IMU was approximately vertical, i.e., the y-z-plane is approximately horizontal. When calculating the angle of the joint axis in this y-z-plane and plotting this angle together with the estimated heading offset δ in Figure 8b, we notice that there is an obvious correlation.

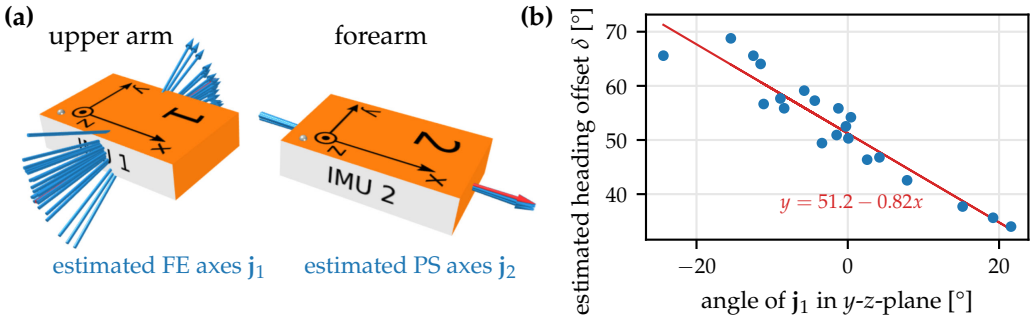

Figure 8. Investigation into the variability of the FE axis estimates (subject 2, complex motion, rotation-based constraint). **(a)** 3D visualization of the axis estimates for all windows. **(b)** Plot of the estimated heading offset δ and the angle of the FE axis in the (approximately horizontal) y-z-plane of the upper arm IMU coordinate system. There is an obvious correlation, indicating that without sufficient upper arm movement, the kinematic constraint does not allow for distinguishing between a heading rotation of the joint axis and a heading offset between the sensor orientations.

This correlation can be explained when considering the kinematic constraint in (7) for the special case in which the upper arm does not move, i.e., the orientation ${}^{\mathcal{B}_1}_{\mathcal{E}_1}\mathbf{q}$ is constant, $\boldsymbol{\omega}_1 = 0$, and the coordinates of $[\mathbf{j}_1]_{\mathcal{E}_1}$ are constant. In this case, there is no difference between a change in δ, i.e., the heading offset between $\mathcal{E}_1$ and $\mathcal{E}_2$, and a rotation of the joint axis estimate $\mathbf{j}_1$ around the vertical axis. The observation in Figure 8 is likely caused by the real situation being too close to this singular case. To mitigate this, care should be taken to avoid calibration motions during which one of the body segments is always stationary.

In summary, the evaluation of the first experiment has shown that the proposed methods yield consistent and plausible joint axis estimates. The rotation-based constraint performs better than the orientation-based constraint. To ensure that the axes converge, the subject's motion should include sufficient motion from both the upper arm and the forearm.

To further enrich the evaluation, we use the data from the first experiment to investigate the influence of the the cutoff frequency for the low-pass filter, the sample selection frequency, and the window duration. The results are presented in Appendix D.

5.2. Accuracy of Magnetometer-Free Joint Angle Tracking

The second experiment is performed to validate that the proposed methods can be used to obtain accurate elbow joint angles for functional motions without relying on a precisely known sensor attachment and without relying on the magnetic field. An optical motion capture system (Vicon Motion Systems Ltd. UK) is used as reference. In addition to the two inertial sensors positioned as in the previous experiment, optical markers are placed on bony landmarks in a way that facilitates joint angle measurement as recommended by the ISB [44]. Note that by placing reflective markers on anatomical landmarks and not, like

Preprints (www.preprints.org) | NOT PEER-REVIEWED | Posted: 2 November 2022 doi:10.20944/preprints202211.0035.v1

many previous works, on the IMUs, we ensure that we compare against the gold standard for measuring joint angles, taking soft tissue motion into account.

Two healthy subjects performed two motions:

1. During the *pick-and-place* motion, the subject placed a small box in a sequence of predefined orientations and locations on a table.
2. The *drinking* motion consists of the subject repeatedly placing the hand on a table, grabbing a cup, simulating a drinking motion, and then placing the cup back on the table.

Each of the four subjects repeats the two motions four times (twice slow and twice fast), resulting in a total of 16 trials, with durations between 14 and 44 s.

For each trial, calculate four different joint angles.

1. The OMC-based *ground truth* angles are derived from the optical markers placed on anatomical landmarks and calculated as described in [44].
2. *Conventional* IMU-based joint angles are calculated using 9D sensor fusion (with the VQF algorithm [47]), i.e., using the magnetic field to determine the heading, and relying on the careful placement of the sensors on the body.
3. In contrast, the *proposed* IMU-based joint angles use 6D sensor fusion (with the VQF algorithm [47]), and the joint axes and heading offset are identified from the trial motion using the
   - *rotation-based* joint constraint and the
   - *orientation-based* joint constraint.

Note that the application of the proposed methods tests the most challenging case, i.e., we use a standard everyday motion to identify both the joint axes and the heading offset without requiring a separate calibration phase.

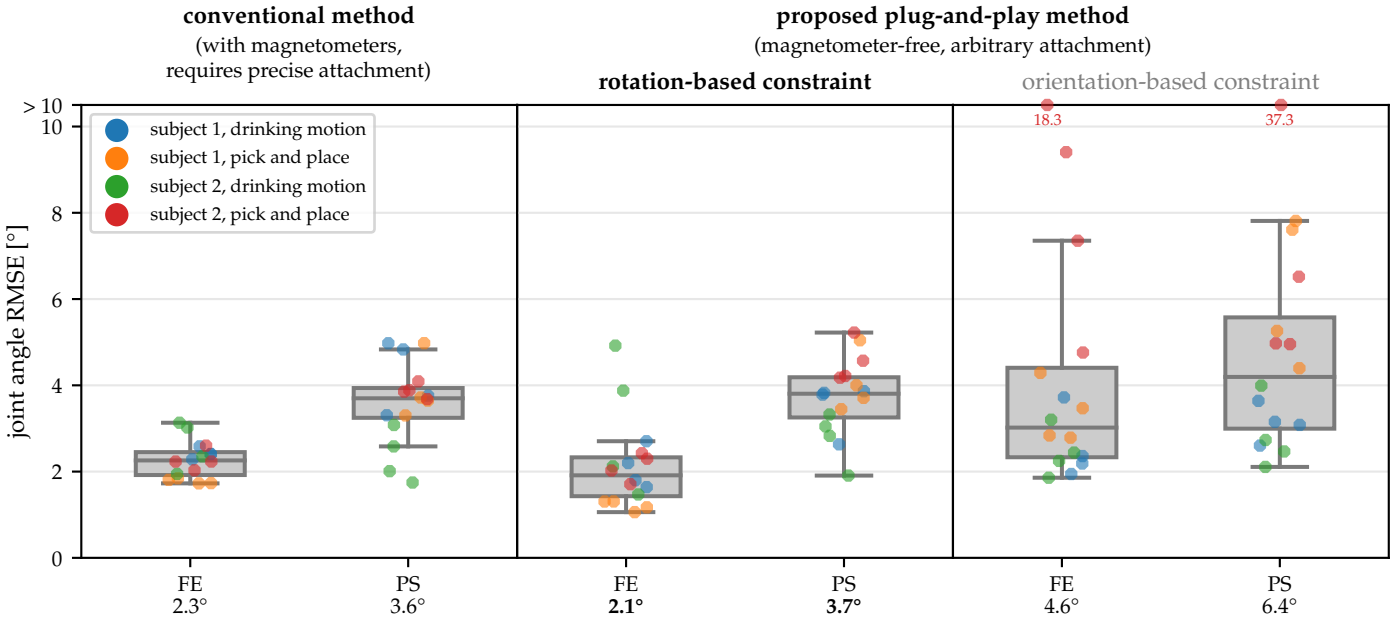

Figure 9. Joint angle estimation errors for all trials with a conventional 9D approach and with the proposed plug-and-play magnetometer-free methods, using OMC-based angles as ground truth. The numbers below the axis labels indicate the mean root mean square error (RMSE) for all 16 trials. The proposed method with the rotation-based constraint yields the same accuracy as the much more restrictive conventional 9D method.

To determine the sign and the required offset for the joint angles, we use the OMC-based angles. The IMU-based joint angles obtained by the different methods are compared

Preprints (www.preprints.org) | NOT PEER-REVIEWED | Posted: 2 November 2022 doi:10.20944/preprints202211.0035.v1

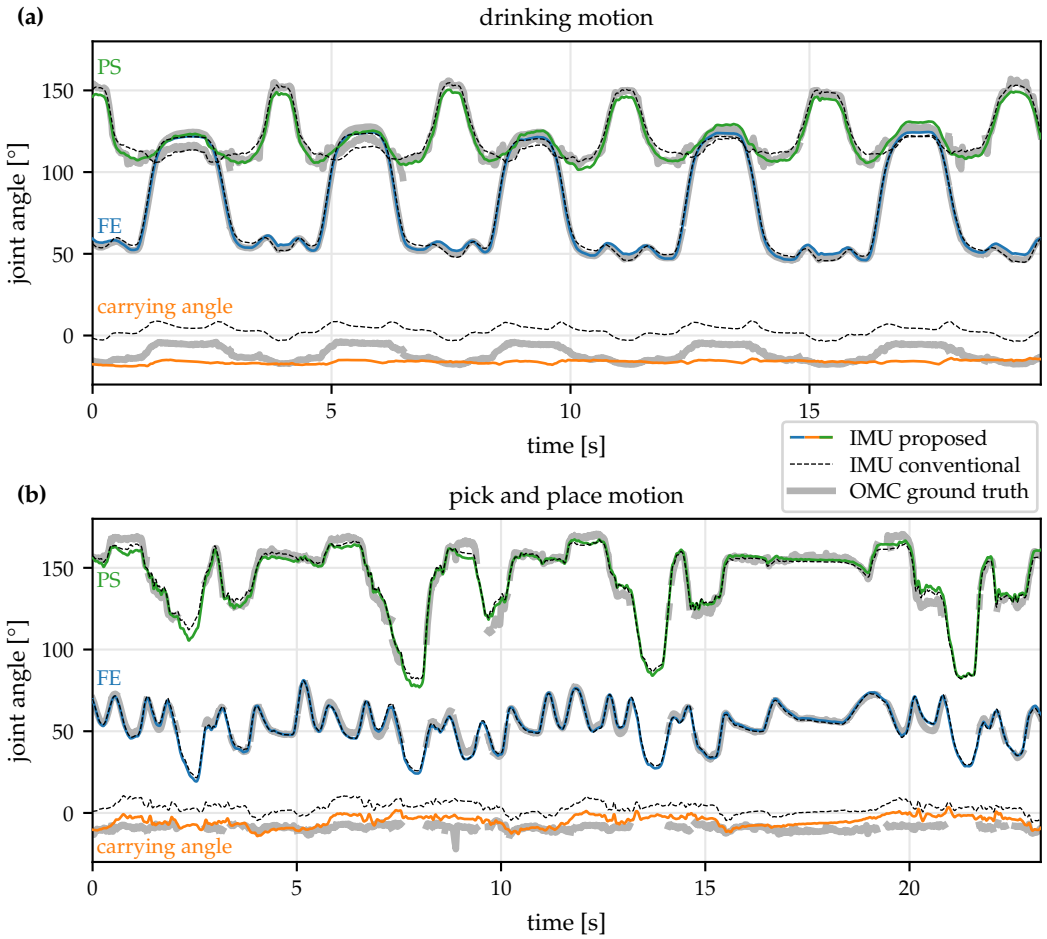

Figure 10. Joint angle trajectories for an exemplary **(a)** drinking and **(b)** pick-and-place trial obtained with the proposed IMU-based method (and the rotation-based constraint), the conventional 9D IMU-based approach, and the OMC ground truth. While being much less restrictive, the proposed method is able to obtain FE and PS joint angles that agree well with the angles obtained with the other two methods.

to the OMC-based ground truth, and the RMSE is calculated. Results from all trials are shown in Figure 9.

When comparing the two variants of the proposed method, we see that the rotation-based constraint outperforms the orientation-based constraint. This coincides with the results of the first experiment presented in Section 5.2. It is noteworthy that for many trials the accuracy achieved with both constraints is comparable and the difference in the mean accuracy is caused by several outliers obtained with the orientation-based constraint, which is consistent with the lower robustness observed for this constraint in Figure 6.

However, when considering the results obtained with the proposed method and the rotation-based constraint, the accuracy is similar to the conventional 9D IMU-based method. For the FE angles, the mean RMSE of 2.1° is 0.2° lower than for the conventional method, while for the PS angles, the mean RMSE of 3.7° is 0.1° larger. In contrast to the results with the orientation-based constraint, there are no outliers, and the maximum RMSE of the proposed method and the conventional method is comparable. Note that the conventional method relies on properly calibrated magnetometer measurements, a controlled environment without ferromagnetic material or electric devices, and a precise and known sensor attachment and is therefore much more restrictive than the proposed magnetometer-free plug-and-play method.

Preprints (www.preprints.org) | NOT PEER-REVIEWED | Posted: 2 November 2022 doi:10.20944/preprints202211.0035.v1

To illustrate the performed motions and the obtained results, Figure 10 shows the OMC ground truth joint angles, the conventional IMU-based joint angles, and the proposed joint angles with the rotation-based constraint for two exemplary trials. As can be seen, the joint angles obtained with the proposed plug-and-play method agree well with both the conventional IMU-based joint angles and the OMC-based ground truth angles.

Note that the joint constraint is only used for identifying the joint axes and that the joint angle calculation uses standard Euler angles and therefore not directly restricted by this constraint. As a result, the obtained carrying angles, which are also shown in Figure 10 but rarely reported in practice, are not perfectly constant.

We can use the carrying angle as an indicator of how well the measured joint motion adheres to the 2-DoF joint model (Figure 3). For a perfect 2-DoF joint, we would expect a perfectly constant carrying angle, while a 3-DoF joint will show significant movement in all three joint angles. Also, if the joint is in fact a 2-DoF joint but the joint axis estimates are wrong, the Euler decomposition will cause variability in all three joint angles.

Therefore, we calculate the standard deviation of the carrying angle as a measure of variability, which is shown in Figure 11 for all 16 trials and all four angle calculation methods. With both constraints, the median of the standard deviations is slightly lower than for the conventional IMU-based joint angles and the OMC-based ground truth. This indicates that the joint axis estimates automatically obtained with the proposed method are better suited to describe the functional motion of the joint than the axes obtained via careful IMU placement and the axes obtained via the placement of optical markers on anatomical landmarks. This agrees with previous research showing that anatomical joint axes defined based on anatomical landmarks do not coincide with the rotation axes of functional joint motion [50]. For joint angle calculation, the use of functional rotation axes seems preferable in order to minimize kinematic cross-talk.

In summary, the evaluation of the second experiment has shown that for the challenging case of using recordings of everyday motions for calibration, the proposed methods are able to obtain joint angles with the same accuracy as a conventional IMU-based approach, while not relying on precise sensor placement or magnetometer measurements. As also shown via the first experiment, the rotation-based constraint performs better than the orientation-based constraint and should therefore be used for anatomical calibration.

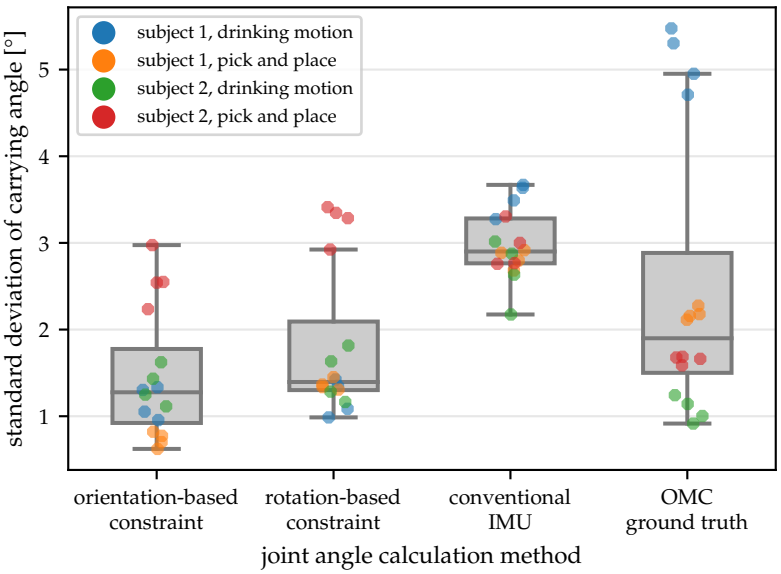

Figure 11. Standard deviation of the carrying angle for all trials with the different angle calculation methods. The proposed method induces the smallest variation in the assumed-to-be-constant carrying angle. This indicates that the estimated joint axes describe the functional motion axes better than the axes obtained via careful manual IMU placement (conventional IMU) and via placing markers on anatomical landmarks (OMC ground truth).

6. Conclusions

The present contribution introduced methods for automatic anatomical calibration for 2-DoF joints, such as the elbow, that do not require the subject to perform precise calibration movements but instead work on arbitrary motions by exploiting one of two kinematic constraints: a rotation-based constraint for the angular rates and an orientation-based constraint. The methods do not make use of magnetometer measurements. Instead, the heading offset is simultaneously estimated via the kinematic constraint, which facilitates plug-and-play magnetometer-free joint angle estimation.

The proposed methods were evaluated using two experiments. The first experiment, without OMC ground truth, showed that the proposed methods yield consistent and plausible joint axis estimates from only ten seconds of motion data. The second experiment, performed with OMC as ground truth, showed that the proposed plug-and-play method can estimate accurate joint angles while being much less restrictive than a conventional IMU-based approach. In both experiments, the rotation-based joint constraint performed better than the orientation-based joint constraint.

The proposed methods overcome mounting and calibration restrictions and facilitate magnetometer-free motion tracking. Therefore, they are highly suitable for indoor environments and improve the practical usability of IMU-based motion tracking in many clinical and biomedical applications.

To further advance the proposed methods, it should be evaluated if combining the rotation-based and the orientation-based constraint can increase the robustness and consistency of the joint axes estimates. Furthermore, introducing and evaluating metrics to quantify the estimation uncertainty and methods for automatic (re-)triggering of the calibration when suitable motions are detected are important next steps to increase the usability of the method.

Author Contributions: Conceptualization, D.L. and T.S.; methodology, D.L. and T.S.; software, D.L.; validation, D.L.; formal analysis, D.L. and T.S.; investigation, D.L.; resources, T.S.; data curation, D.L.; writing—original draft preparation, D.L.; writing—review and editing, D.L., I.W. and T.S.; visualization, D.L.; supervision, T.S.; project administration, T.S.; funding acquisition, T.S. All authors have read and agreed to the published version of the manuscript.

Funding: This research received no external funding.

Institutional Review Board Statement: Not applicable.

Informed Consent Statement: Informed consent was obtained from all subjects involved in the study.

Data Availability Statement: The data presented in this study is available on request from the corresponding author.

Acknowledgments: We thank Johanna Carstensen and Lars Nienerowski for their skillful support in conducting the experiments and processing the data.

Conflicts of Interest: The authors declare no conflict of interest.

Abbreviations

The following abbreviations are used in this manuscript:

 doi:10.20944/preprints202211.0035.v1

6D	sensor fusion with gyroscope and accelerometer data
9D	sensor fusion with gyroscope, accelerometer, and magnetometer data
DoF	degrees of freedom
FE	flexion and extension
IMU	inertial measurement unit
IOE	inertial orientation estimation
ISB	International Society of Biomechanics
MCP	metacarpophalangeal joint
OMC	optical motion capture
PS	pronation and supination
RMSE	root mean square error

Appendix A. Transforming Any General 2D Joint Model to Euler Angles

The proposed methods for automatic anatomical calibration use z-y'-x'' Euler angles to decompose the relative segment orientation into joint angles. This decomposition was chosen because it is recommended by the ISB for the elbow [44]. However, this choice is not restrictive in any way. In the following, we show that any joint model with two degrees of freedom can be transformed to fit the chosen Euler angle representation. For example, instead of using regular Euler angles, we could consider modeling a 2-DoF joint with axes that are all potentially non-orthogonal (including the carrying angle axis), i.e.,

$$\prescript{\mathcal{B}_2'}{\mathcal{B}_1'}{\mathbf{q}} = (\alpha'(t) \mathbin{@} \mathbf{j}_1') \otimes \left(\beta_0' \mathbin{@} \mathbf{j}_\beta'\right) \otimes (\gamma'(t) \mathbin{@} \mathbf{j}_2'), \tag{A1}$$

or assume that the relative segment orientation is a sequence of two non-orthogonal rotations (which is a special case of the above model with $\beta' = 0$). Furthermore, the joint model might include additional fixed rotations, similar to the carrying angle, at the beginning or at the end of the rotation sequence.

To capture all those possibilities, we start with a very general model of a joint with two degrees of freedom, described as the decomposition of the relative body segment orientation quaternion

$$\prescript{\mathcal{B}_2'}{\mathcal{B}_1'}{\mathbf{q}} = \mathbf{q}_1 \otimes (\alpha \mathbin{@} \mathbf{j}_1) \otimes \mathbf{q}_2 \otimes (\gamma \mathbin{@} \mathbf{j}_2) \otimes \mathbf{q}_3. \tag{A2}$$

The 3D vectors $\mathbf{j}_1$ and $\mathbf{j}_2$ are arbitrary but constant joint rotation axes, $\alpha(t)$ and $\gamma(t)$ are the two time-varying joint angles, and $\mathbf{q}_1$, $\mathbf{q}_2$ and $\mathbf{q}_3$ are arbitrary but constant rotations.

Without loss of generality, we can write $(\alpha \mathbin{@} \mathbf{j}_1) = \mathbf{q}_4 \otimes (\alpha \mathbin{@} [0\ 0\ 1]^\intercal) \otimes \mathbf{q}_4^{-1}$ and $(\gamma \mathbin{@} \mathbf{j}_2) = \mathbf{q}_5 \otimes (\alpha \mathbin{@} [0\ 1\ 0]^\intercal) \otimes \mathbf{q}_5^{-1}$, with some constant rotations $\mathbf{q}_4$, $\mathbf{q}_5$ that rotate between the given joint axes and the z-axis and y-axis, respectively. Inserting this into (A2) gives

$$\prescript{\mathcal{B}_2'}{\mathcal{B}_1'}{\mathbf{q}} = \mathbf{q}_1 \otimes \mathbf{q}_4 \otimes (\alpha \mathbin{@} [0\ 0\ 1]^\intercal) \otimes \mathbf{q}_4^{-1} \otimes \mathbf{q}_2 \otimes \mathbf{q}_5 \otimes (\gamma \mathbin{@} [0\ 1\ 0]^\intercal) \otimes \mathbf{q}_5^{-1} \otimes \mathbf{q}_3. \tag{A3}$$

Since we can decompose any quaternion into Euler angles, we can write

$$\mathbf{q}_4^{-1} \otimes \mathbf{q}_2 \otimes \mathbf{q}_5 = (\alpha_0 \mathbin{@} [0\ 0\ 1]^\intercal) \otimes (\beta_0 \mathbin{@} [1\ 0\ 0]^\intercal) \otimes (\gamma_0 \mathbin{@} [0\ 1\ 0]^\intercal). \tag{A4}$$

Furthermore, we can define new body segment coordinate systems $\mathcal{B}_1$ and $\mathcal{B}_2$:

$$\prescript{\mathcal{B}_1}{\mathcal{B}_1'}{\mathbf{q}} = \mathbf{q}_1 \otimes \mathbf{q}_4 \tag{A5}$$

$$\prescript{\mathcal{B}_2'}{\mathcal{B}_2}{\mathbf{q}} = \mathbf{q}_5^{-1} \otimes \mathbf{q}_3. \tag{A6}$$

Preprints (www.preprints.org) | NOT PEER-REVIEWED | Posted: 2 November 2022 doi:10.20944/preprints202211.0035.v1

Putting (A4), (A5) and (A5) into (A3) yields

$$\begin{aligned} {}^{\mathcal{B}_2}_{\mathcal{B}_1}\mathbf{q} &= (\alpha\,@\,[0\ 0\ 1]^\intercal) \otimes \mathbf{q}_4^{-1} \otimes \mathbf{q}_2 \otimes \mathbf{q}_5 \otimes (\gamma\,@\,[0\ 1\ 0]^\intercal) && \text{(A7)} \\ &= (\alpha+\alpha_0\,@\,[0\ 0\ 1]^\intercal) \otimes (\beta_0\,@\,[1\ 0\ 0]^\intercal) \otimes (\gamma+\gamma_0\,@\,[0\ 1\ 0]^\intercal). && \text{(A8)} \end{aligned}$$

This represents z-x'-y'' Euler angles as recommended for the elbow by [44], with a constant carrying angle β_0. The time-varying joint angles in the generic model (A2) and in the Euler angle model (A8) are only shifted by constant offsets α_0 and γ_0. Therefore, without loss of generality, all joints that can be represented with two sequential rotations around arbitrary but constant axes can be described using z-x'-y'' Euler angles.

Appendix B. Details on the Optimization Procedure

Appendix B.1. Gauss-Newton Algorithm

To estimate the joint axes $\mathbf{j}_1$ and $\mathbf{j}_2$ and the heading offset δ given a set of M samples, we find the parameter vector $\hat{\mathbf{\Phi}}$ that minimizes the sum of squares, i.e.,

$$\hat{\mathbf{\Phi}} = \arg\min_{\mathbf{\Phi}} \sum_{t_k \in B} e(t_k)^2 = \arg\min_{\mathbf{\Phi}} \mathbf{e}^\intercal \mathbf{e}, \tag{A9}$$

with $\mathbf{e} \in \mathbb{R}^{M\times 1}$ being the error vector and B denoting the set of sampling times t_k in the buffer.

For any given parameter vector, we can evaluate the Jacobian $\mathbf{J} \in \mathbb{R}^{M\times 5}$ with

$$[\mathbf{J}]_{ij} = \frac{\partial e_i}{\partial \Phi_j}. \tag{A10}$$

Analytical expressions for all elements of $\mathbf{J}$ that only depend on the parameters $\mathbf{\Phi}$ and on the measurements are given in Appendix B.3 for the rotation-based constraint and in Appendix B.4 for the orientation-based constraint.

The Gauss-Newton algorithm [49] is used to minimize the error. Starting with an initial parameter vector $\mathbf{\Phi}_0$, we iteratively obtain the estimate by

$$\mathbf{\Phi}_{i+1} = \mathbf{\Phi}_i + \alpha \mathbf{p}_\mathrm{i} \text{ with } \mathbf{J}^\intercal \mathbf{J} \mathbf{p}_\mathrm{i} = \mathbf{J}^\intercal \mathbf{e}, \tag{A11}$$

until convergence is achieved, with the iteration index i, the step direction $\mathbf{p}_\mathrm{i}$, and the step length $\alpha = 1$. In between iterations, we switch from one joint axis representation to the other via Cartesian coordinates if $|\sin\theta_i| < \frac{1}{2}$, $i = 1, 2$ (cf. Figure 4). As a result of the optimization step, we obtain the joint axes $\mathbf{j}_1$ and $\mathbf{j}_2$ in the coordinates systems of sensors $\mathcal{S}_1$ and $\mathcal{S}_2$, respectively, and the heading offset δ between the reference frames $\mathcal{E}_1$ and $\mathcal{E}_2$.

Appendix B.2. Moving Window Approach for Real-Time Applications

Note that the proposed optimization method can not only be applied to recorded datasets but is also suitable for real-time application. In the simplest case, samples are saved while the subject performs a motion and afterward, the optimization is performed on the stored samples, and the resulting calibration parameters are applied to all subsequent samples. For an improved online implementation that continuously updates the axes estimates (if desired) and that starts to provide estimates as early as possible, the method can be extended to the following moving window approach:

1. New samples are continuously selected every 0.05 s and stored in a ring buffer containing $M = 200$ data sets, i.e., old data sets are automatically discarded.
2. As soon as the buffer is half-full, optimization starts.
3. One Gauss-Newton step is performed every time a sample is added to the buffer (to continuously update the solution while spreading the computational load over time).

Preprints (www.preprints.org) | NOT PEER-REVIEWED | Posted: 2 November 2022 doi:10.20944/preprints202211.0035.v1

Note that it is also possible to keep the parameters for the joint axes θ_1, φ_1, θ_2, and φ_2 fixed after the initial estimate and only track the heading offset δ.

Appendix B.3. Gradient of Rotation-Based Cost Function

For efficient optimization using the rotation-based joint constraint introduced in Section 4.2, we need to calculate the elements of the Jacobian $\mathbf{J}$, i.e.,

$$[\mathbf{J}]_{ij} = \frac{\partial e_i}{\partial \Phi_j} = \boldsymbol{\omega}_{\text{rel}} \cdot \frac{\partial}{\partial \Phi_j} \frac{\mathbf{j}_\text{n}}{\|\mathbf{j}_\text{n}\|} + \frac{\mathbf{j}_\text{n}}{\|\mathbf{j}_\text{n}\|} \cdot \frac{\partial}{\partial \Phi_j} \boldsymbol{\omega}_{\text{rel}}. \tag{A12}$$

The derivative of the normalized axis is

$$\frac{\partial}{\partial \Phi_j} \frac{\mathbf{j}_\text{n}}{\|\mathbf{j}_\text{n}\|} = \frac{\frac{\partial}{\partial \Phi_j}\mathbf{j}_\text{n}}{\|\mathbf{j}_\text{n}\|} - \mathbf{j}_\text{n} \frac{\mathbf{j}_\text{n} \cdot \frac{\partial}{\partial \Phi_j}\mathbf{j}_\text{n}}{\|\mathbf{j}_\text{n}\|^3}. \tag{A13}$$

All necessary subsequent derivatives are detailed in the following. Note that, while $\mathbf{j}_\text{n}$ depends on all parameters in $\boldsymbol{\Phi}$, the relative angular rate $\boldsymbol{\omega}_{\text{rel}}$ only depends on δ.

Appendix B.3.1. Derivative with Respect to the Joint Axes

We exploit the fact that the product rule holds for quaternion multiplication [51, p. 24].[3]

$$\frac{\partial \mathbf{j}_\text{n}}{\partial \theta_1, \varphi_1} = \left({}^{\mathcal{S}_1}_{\mathcal{E}_1}\mathbf{q} \otimes \frac{\partial}{\partial \theta_1, \varphi_1} \mathbf{j}_1 \otimes {}^{\mathcal{S}_1}_{\mathcal{E}_1}\mathbf{q}^{-1} \right) \times [\mathbf{j}_2]_{\mathcal{E}_1} \tag{A14}$$

$$\frac{\partial \mathbf{j}_\text{n}}{\partial \theta_2, \varphi_2} = [\mathbf{j}_1]_{\mathcal{E}_1} \times \left({}^{\mathcal{S}_2}_{\mathcal{E}_1}\mathbf{q} \otimes \frac{\partial}{\partial \theta_2, \varphi_2} \mathbf{j}_2 \otimes {}^{\mathcal{S}_2}_{\mathcal{E}_1}\mathbf{q}^{-1} \right) \tag{A15}$$

Deriving the axes in local sensor coordinates with respect to θ and φ as defined in (14) is straightforward:

$$\frac{\partial \mathbf{j}_\text{i}}{\partial \theta_i} = [\cos\theta_i \cos\varphi_i \quad \cos\theta_i \sin\varphi_i \quad -\sin\theta_i\,]^\intercal, \tag{A16}$$

$$\frac{\partial \mathbf{j}_\text{i}}{\partial \varphi_i} = [-\sin\theta_i \sin\varphi_i \quad \sin\theta_i \cos\varphi_i \quad 0\,]^\intercal, \quad i = 1, 2. \tag{A17}$$

The same is possible for the alternative joint axis parametrization.

Appendix B.3.2. Derivative with Respect to the Heading Offset

Instead of quaternion multiplication, we can make use of Rodrigues' rotation formula to express the transformation of a vector $\mathbf{v} \in \mathbb{R}^3$ from $\mathcal{E}_2$ to $\mathcal{E}_1$, i.e.,

$$[\mathbf{v}]_{\mathcal{E}1} = {}^{\mathcal{E}_2}_{\mathcal{E}_1}\mathbf{q} \otimes [\mathbf{v}]_{\mathcal{E}_2} \otimes {}^{\mathcal{E}_2}_{\mathcal{E}_1}\mathbf{q}^{-1} \tag{A18}$$

$$= [\mathbf{v}]_{\mathcal{E}_2} \cos(\delta) + \left([0 \;\; 0 \;\; 1]^\intercal \times [\mathbf{v}]_{\mathcal{E}_2} \right) \sin(\delta) + [0 \;\; 0 \;\; 1]^\intercal \left([0 \;\; 0 \;\; 1]^\intercal \cdot [\mathbf{v}]_{\mathcal{E}_2} \right) (1 - \cos(\delta)). \tag{A19}$$

[3] Similarly, we could argue that the rotation can be expressed using a rotation matrix and make use of the product rule for matrix multiplication.

Preprints (www.preprints.org) | NOT PEER-REVIEWED | Posted: 2 November 2022 doi:10.20944/preprints202211.0035.v1

This allows us to calculate the derivatives

$$\frac{\partial \boldsymbol{\omega}_{\text{rel}}}{\partial \delta} = -\frac{\partial}{\partial \delta}[\boldsymbol{\omega}_2]_{\mathcal{E}_1} \tag{A20}$$

$$= [\boldsymbol{\omega}_2]_{\mathcal{E}_2}\sin(\delta) - \left([0\ 0\ 1]^\intercal \times [\boldsymbol{\omega}_2]_{\mathcal{E}_2}\right)\cos(\delta) - [0\ 0\ 1]^\intercal\left([0\ 0\ 1]^\intercal \cdot [\boldsymbol{\omega}_2]_{\mathcal{E}_2}\right)\sin(\delta) \tag{A21}$$

and

$$\frac{\partial \mathbf{j}_{\text{n}}}{\partial \delta} = [\mathbf{j}_1]_{\mathcal{E}_1} \times \frac{\partial}{\partial \delta}[\mathbf{j}_2]_{\mathcal{E}_1} \text{with} \tag{A22}$$

$$\frac{\partial}{\partial \delta}[\mathbf{j}_2]_{\mathcal{E}_1} = -[\mathbf{j}_2]_{\mathcal{E}2}\sin(\delta) + \left([0\ 0\ 1]^\intercal \times [\mathbf{j}_2]_{\mathcal{E}_2}\right)\cos(\delta) + [0\ 0\ 1]^\intercal\left([0\ 0\ 1]^\intercal \cdot [\mathbf{j}_2]_{\mathcal{E}_2}\right)\sin(\delta). \tag{A23}$$

Appendix B.4. Gradient of Orientation-Based Cost Function

Analogously to the derivation in Section B.3, we now show how to calculate the elements of the Jacobian $\mathbf{J}$ for the orientation-based constraint introduced in Section 4.2, i.e.,

$$[\mathbf{J}]_{ij} = \frac{\partial e_i}{\partial \Phi_j} = \frac{\partial}{\partial \Phi_j}\Big(\arcsin\underbrace{\left(2q_w q_x + 2q_y q_z\right)}_{=:\,s(\theta_1,\varphi_1,\theta_2,\varphi_2,\delta)} - \beta_0\Big), \tag{A24}$$

with ${}^{\mathcal{B}_2}_{\mathcal{B}_1}\mathbf{q} =: [q_w\ \ q_x\ \ q_y\ \ q_z]^\intercal$.

Trivially, the derivative with respect to the fixed carrying angle β_0 is

$$\frac{\partial e_i}{\partial \beta_0} = -1. \tag{A25}$$

For the derivatives with respect to the other parameters, we make use of the fact that

$$\frac{\partial}{\partial \Phi_j}\arcsin s(\Phi_j) = \frac{\frac{\partial}{\partial \Phi_j}s(\Phi_j)}{\sqrt{1 - s(\Phi_j)^2}} \tag{A26}$$

and that

$$\frac{\partial}{\partial \Phi_j}s(\Phi_j) = 2\left(\frac{\partial q_x}{\partial \Phi_j}q_w + q_x\frac{\partial q_w}{\partial \Phi_j} + \frac{\partial q_y}{\partial \Phi_j}q_z + q_y\frac{\partial q_z}{\partial \Phi_j}\right). \tag{A27}$$

To determine the derivative of the quaternion components q_w, q_x, q_y, and q_z, remember that the relative segment orientation ${}^{\mathcal{B}_2}_{\mathcal{B}_1}\mathbf{q}$, as defined in (11), is the multiplicative concatenation of five quaternions:

$${}^{\mathcal{B}_2}_{\mathcal{B}_1}\mathbf{q} = {}^{\mathcal{S}_1}_{\mathcal{B}_1}\mathbf{q}(\theta_1,\varphi_1) \otimes {}^{\mathcal{E}_1}_{\mathcal{S}_1}\mathbf{q} \otimes {}^{\mathcal{E}_2}_{\mathcal{E}_1}\mathbf{q}(\delta) \otimes {}^{\mathcal{S}_2}_{\mathcal{E}_2}\mathbf{q} \otimes {}^{\mathcal{B}_2}_{\mathcal{S}_2}\mathbf{q}(\theta_2,\varphi_2). \tag{A28}$$

Since for each parameter, only a single of those five quaternions depends on the respective parameter, the other four quaternions are constant factors, i.e.,

$$\frac{\partial}{\partial \theta_1,\varphi_1}{}^{\mathcal{B}_2}_{\mathcal{B}_1}\mathbf{q} = \left(\frac{\partial}{\partial \theta_1,\varphi_1}{}^{\mathcal{S}_1}_{\mathcal{B}_1}\mathbf{q}\right) \otimes {}^{\mathcal{E}_1}_{\mathcal{S}_1}\mathbf{q} \otimes {}^{\mathcal{E}_2}_{\mathcal{E}_1}\mathbf{q} \otimes {}^{\mathcal{S}_2}_{\mathcal{E}_2}\mathbf{q} \otimes {}^{\mathcal{B}_2}_{\mathcal{S}_2}\mathbf{q} \tag{A29}$$

$$\frac{\partial}{\partial \delta}{}^{\mathcal{B}_2}_{\mathcal{B}_1}\mathbf{q} = {}^{\mathcal{S}_1}_{\mathcal{B}_1}\mathbf{q} \otimes {}^{\mathcal{E}_1}_{\mathcal{S}_1}\mathbf{q} \otimes \left(\frac{\partial}{\partial \delta}{}^{\mathcal{E}_2}_{\mathcal{E}_1}\mathbf{q}\right) \otimes {}^{\mathcal{S}_2}_{\mathcal{E}_2}\mathbf{q} \otimes {}^{\mathcal{B}_2}_{\mathcal{S}_2}\mathbf{q} \tag{A30}$$

$$\frac{\partial}{\partial \theta_2,\varphi_2}{}^{\mathcal{B}_2}_{\mathcal{B}_1}\mathbf{q} = {}^{\mathcal{S}_1}_{\mathcal{B}_1}\mathbf{q} \otimes {}^{\mathcal{E}_1}_{\mathcal{S}_1}\mathbf{q} \otimes {}^{\mathcal{E}_2}_{\mathcal{E}_1}\mathbf{q} \otimes {}^{\mathcal{S}_2}_{\mathcal{E}_2}\mathbf{q} \otimes \left(\frac{\partial}{\partial \theta_2,\varphi_2}{}^{\mathcal{B}_2}_{\mathcal{S}_2}\mathbf{q}\right). \tag{A31}$$

Preprints (www.preprints.org) | NOT PEER-REVIEWED | Posted: 2 November 2022 doi:10.20944/preprints202211.0035.v1

Appendix B.4.1. Derivative with Respect to the Joint Axes

The sensor-to-segment orientation for the first segment can be expressed as

$$ {}^{\mathcal{S}_1}_{\mathcal{B}_1}\mathbf{q} = \begin{bmatrix} \cos(\frac{\psi}{2}) \\ \sin(\frac{\psi}{2})\frac{\mathbf{v}}{\|\mathbf{v}\|} \end{bmatrix}, \text{ with } \psi = \arccos(j_{1,z}) \text{ and } \mathbf{v} = \mathbf{j}_1 \times \begin{bmatrix} 0 \\ 0 \\ 1 \end{bmatrix} = \begin{bmatrix} j_{1,y} \\ -j_{1,x} \\ 0 \end{bmatrix}. \tag{A32} $$

For the scalar part of the quaternion,

$$ \frac{\partial}{\partial \theta_1, \varphi_1} \cos\left(\frac{\psi}{2}\right) = -\frac{1}{2}\sin\left(\frac{\psi}{2}\right)\frac{\partial \psi}{\partial \theta_1, \varphi_1} \tag{A33} $$

and

$$ \frac{\partial}{\partial \theta_1, \varphi_1}\psi = -\frac{\frac{\partial j_{1,z}}{\partial \theta_1, \varphi_1}}{\sqrt{1 - j_{1,z}^2}}. \tag{A34} $$

The derivative of the vector part of the quaternion is

$$ \frac{\partial}{\partial \theta_1, \varphi_1}\sin\left(\frac{\psi}{2}\right)\frac{\mathbf{v}}{\|\mathbf{v}\|} = \frac{1}{\|\mathbf{v}\|^2}\left(\mathbf{v}\|\mathbf{v}\|\frac{\partial \sin(\frac{\psi}{2})}{\partial \theta_1, \varphi_1} + \sin\left(\frac{\psi}{2}\right)\|\mathbf{v}\|\frac{\partial \mathbf{v}}{\partial \theta_1, \varphi_1} - \sin\left(\frac{\psi}{2}\right)\mathbf{v}\frac{\partial \|\mathbf{v}\|}{\partial \theta_1, \varphi_1}\right), \tag{A35} $$

with

$$ \frac{\partial}{\partial \theta_1, \varphi_1}\sin\left(\frac{\psi}{2}\right) = \frac{1}{2}\cos\left(\frac{\psi}{2}\right)\frac{\partial \psi}{\partial \theta_1, \varphi_1} \tag{A36} $$

and

$$ \frac{\partial}{\partial \theta_1, \varphi_1}\|\mathbf{v}\| = \frac{1}{\|\mathbf{v}\|}\left(j_{1,y}\frac{\partial j_{1,y}}{\partial \theta_1, \varphi_1} - j_{1,x}\frac{\partial j_{1,x}}{\partial \theta_1, \varphi_1}\right). \tag{A37} $$

For the derivatives of the Cartesian joint axis vector $\mathbf{j}_1$ with respect to θ_1 and φ_1, refer to Appendix B.3.

The derivative with respect to θ_2 and φ_2 follows analogously for the second sensor-to-segment orientation

$$ {}^{\mathcal{B}_2}_{\mathcal{S}_2}\mathbf{q} = \begin{bmatrix} \cos(\frac{\psi}{2}) \\ \sin(\frac{\psi}{2})\frac{\mathbf{v}}{\|\mathbf{v}\|} \end{bmatrix}, \text{ with } \psi = \arccos(j_{2,x}) \text{ and } \mathbf{v} = \begin{bmatrix} 0 \\ 1 \\ 0 \end{bmatrix} \times \mathbf{j}_2 = \begin{bmatrix} j_{1,z} \\ 0 \\ -j_{1,x} \end{bmatrix}. \tag{A38} $$

Appendix B.4.2. Derivative with Respect to the Heading Offset

The derivative of the heading offset quaternion

$$ {}^{\mathcal{E}_2}_{\mathcal{E}_1}\mathbf{q} = \begin{bmatrix} \cos(\frac{\delta}{2}) & 0 & 0 & \sin(\frac{\delta}{2}) \end{bmatrix}^\mathsf{T} \tag{A39} $$

with respect to the heading offset δ is

$$ \frac{\partial}{\partial \delta}{}^{\mathcal{E}_2}_{\mathcal{E}_1}\mathbf{q} = \begin{bmatrix} -\frac{1}{2}\sin(\frac{\delta}{2}) & 0 & 0 & \frac{1}{2}\cos(\frac{\delta}{2}) \end{bmatrix}^\mathsf{T}. \tag{A40} $$

Appendix C. On-Chip Sensor Fusion, Soft Tissue Motions, and Axis Ambiguity

Appendix C.1. Extension to On-Chip 6D Sensor Fusion

Especially in wireless inertial sensor networks, it is desirable to perform on-chip sensor fusion, potentially with a high sampling rate of the gyroscopes, and then to only transmit

Preprints (www.preprints.org) | NOT PEER-REVIEWED | Posted: 2 November 2022 doi:10.20944/preprints202211.0035.v1

the orientation quaternions at a regular (and typically much lower) sampling rate to the processing unit. However, the constraint (7) is based on angular rates, i.e., on the gyroscope measurements.

Instead of transmitting the gyroscope measurements as well, which requires extra bandwidth, increases power consumption, and might not be possible without changing hardware and/or the communication protocol, the angular rates can easily be approximated from the change of orientation

$$\left[{}^{\mathcal{S}_i(t_k)}_{\mathcal{S}_i(t_{k-1})}\mathbf{q}\right]_{\mathcal{E}_i} = {}^{\mathcal{S}_i(t_k)}_{\mathcal{E}_i}\mathbf{q} \otimes {}^{\mathcal{S}_i(t_{k-1})}_{\mathcal{E}_i}\mathbf{q}^{-1} =: [\,q_w \;\; q_x \;\; q_y \;\; q_z\,]^\intercal, \quad i = 1,2, \tag{A41}$$

by

$$[\boldsymbol{\omega}(t_k)]_{\mathcal{E}_i} = \frac{2}{T_\mathrm{s}} \arccos(q_w) \frac{[\,q_x \;\; q_y \;\; q_z\,]^\intercal}{\left\|[\,q_x \;\; q_y \;\; q_z\,]^\intercal\right\|}. \tag{A42}$$

Note that due to the order of quaternion multiplication, we already obtain the angular rate in each sensor's global frame, thus avoiding another transformation step.

Of course, when the gyroscope and accelerometer readings are available, it is equally possible to perform 6D sensor fusion in the processing unit, e.g., using the VQF algorithm [47], and directly employ the angular rates measured by the gyroscopes for evaluation of the kinematic constraint. Therefore, this proposed extension is not restrictive but instead broadens the scope of applicability of the method.

Note that the orientation-based constraint is already quaternion-based and does not require any other measurement data. Therefore, employing the proposed extension is not necessary when using this constraint.

Appendix C.2. Measurement and Soft Tissue Motion Artifact Reduction

Measurement anomalies, such as the sensor accidentally touching objects, or soft tissue motion can cause artifacts in the measured angular rates $\boldsymbol{\omega}_1$ and $\boldsymbol{\omega}_2$. This leads to high-frequency disturbances (compared to the frequency of the functional joint motions) that often violate the rotation-based constraint (7) and therefore deteriorate the estimation accuracy. Low-pass filtering of the angular rates used for evaluating the rotation-based constraint with a cutoff frequency of $f_\mathrm{c} = 5\,\mathrm{Hz}$ improves the accuracy and robustness of the anatomical calibration.

Appendix C.3. Ambiguity in the Signs of the Joint Axes

The joint constraints cannot be used to determine the signs of the joint rotation axes, as for any pair of axes, the value of the cost function for $(\mathbf{j}_1, \mathbf{j}_2)$, $(-\mathbf{j}_1, -\mathbf{j}_2)$ and also $(\mathbf{j}_1, -\mathbf{j}_2)$ is exactly the same. Correspondingly, whether, for example, supination is defined as a positive or negative rotation around an axis pointing proximally along the right forearm is only a matter of convention.

In practical applications, it is essential to ensure that a specific definition is always followed, e.g., [44]. In order to determine the sign, two approaches are practical: The first is to ensure a sensor placement that is roughly known, i.e., the half-space in which each joint axis points is predetermined. Another way is to exploit the joint's range of motion in combination with the offset-removal method described in Section 4.5. For example, by defining that an extended and supinated elbow corresponds to $\alpha = 0, \gamma = 0$ and choosing the signs of the axes so that the mean joint angles during calibration are positive, we ensure that we follow the definitions given in [44].

Appendix D. Sensitivity to Cutoff Frequency, Sample Selection Frequency, and Window Duration

As a further part of the evaluation, we consider the three main degrees of freedom in applying the proposed methods and investigate the influence of those parameters:

Preprints (www.preprints.org) | NOT PEER-REVIEWED | Posted: 2 November 2022 doi:10.20944/preprints202211.0035.v1

- the cutoff frequency f_c for measurement and soft tissue motion artifact reduction (employed value: 5 Hz, cf. Appendix C.2, rotation-based constraint only)
- the sample selection frequency (employed value: 20 Hz, $T_s = 0.05$ s)
- the duration of the measurement window (employed value: 10 s).

We apply the proposed methods to all trials of the five subjects of the first experiment for different values of the respective parameter while keeping the other two parameters at the previously employed default value. In order to condense the obtained information (cf. Figure 6), we calculate the mean and the 99th percentile of the variability angles ε_w of all windows of all trials.

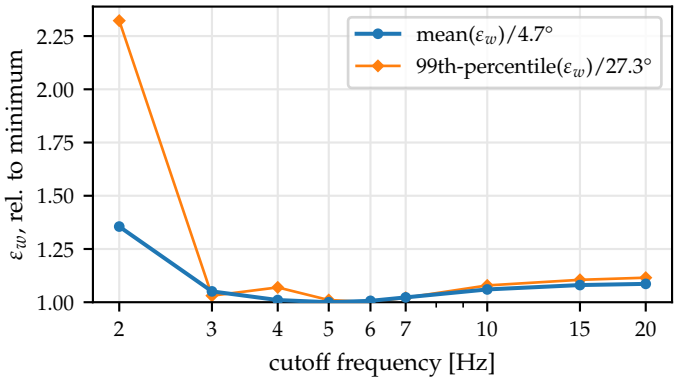

Figure A1. Variability of the obtained axis estimates (mean and 99th-percentile of ε_w, relative to minimum value) for different values of the cutoff frequency of the soft tissue motion artifact reduction low pass filter. Low-pass filtering of the angular rates increases the consistency of the axis estimates, but for too low cutoff frequencies, important information gets lost, and the deviations increase. Choosing a cutoff frequency of 5 Hz gives robust estimates.

For the angular rate cutoff frequency f_c for measurement and soft tissue motion artifact reduction, the obtained results are shown in Figure A1. If the cutoff frequency is chosen too low ($f_c = 2$ Hz), the mean and 99th-percentile of ε_w increase compared to the smallest possible value. At those frequencies, valuable information about the movement gets lost, leading to more inconsistent estimation results. However, when choosing $3\,\text{Hz} \leq f_c \leq 7\,\text{Hz}$, the results are more consistent than without low-pass filter. Therefore, we can conclude that low-pass filtering of the angular rates helps to increase robustness and that $f_c = 5$ Hz is a reasonable choice for the cutoff frequency.

To determine how much data is needed to get consistent estimates, we repeat the same evaluation for the other two parameters, i.e., window duration and sample selection frequency, which is shown for both constraints in Figure A2. As expected, using more data in the optimization, i.e., increasing the window duration or increasing the sample selection frequency, leads to more consistent estimates. However, this comes at a cost. Longer window durations cause inconvenience for the subject that has to perform the movements and limit the applicability of the method. Therefore, the duration of 10 s was chosen as a compromise between ease of use and accuracy and to demonstrate that such short durations lead to good results. If the data is available, employing longer motion sequences should be considered (up to a point where the assumption of δ being constant is not valid anymore due to integration drift). The sampling selection frequency is less critical as it only affects the computational time. However, the results show that increasing the frequency past 10 Hz does not significantly affect the results. The chosen frequency of 20 Hz is more than sufficient while still considerably removing the number of data sets compared to typical IMU raw data sampling rates of 50–500 Hz.

Preprints (www.preprints.org) | NOT PEER-REVIEWED | Posted: 2 November 2022 doi:10.20944/preprints202211.0035.v1

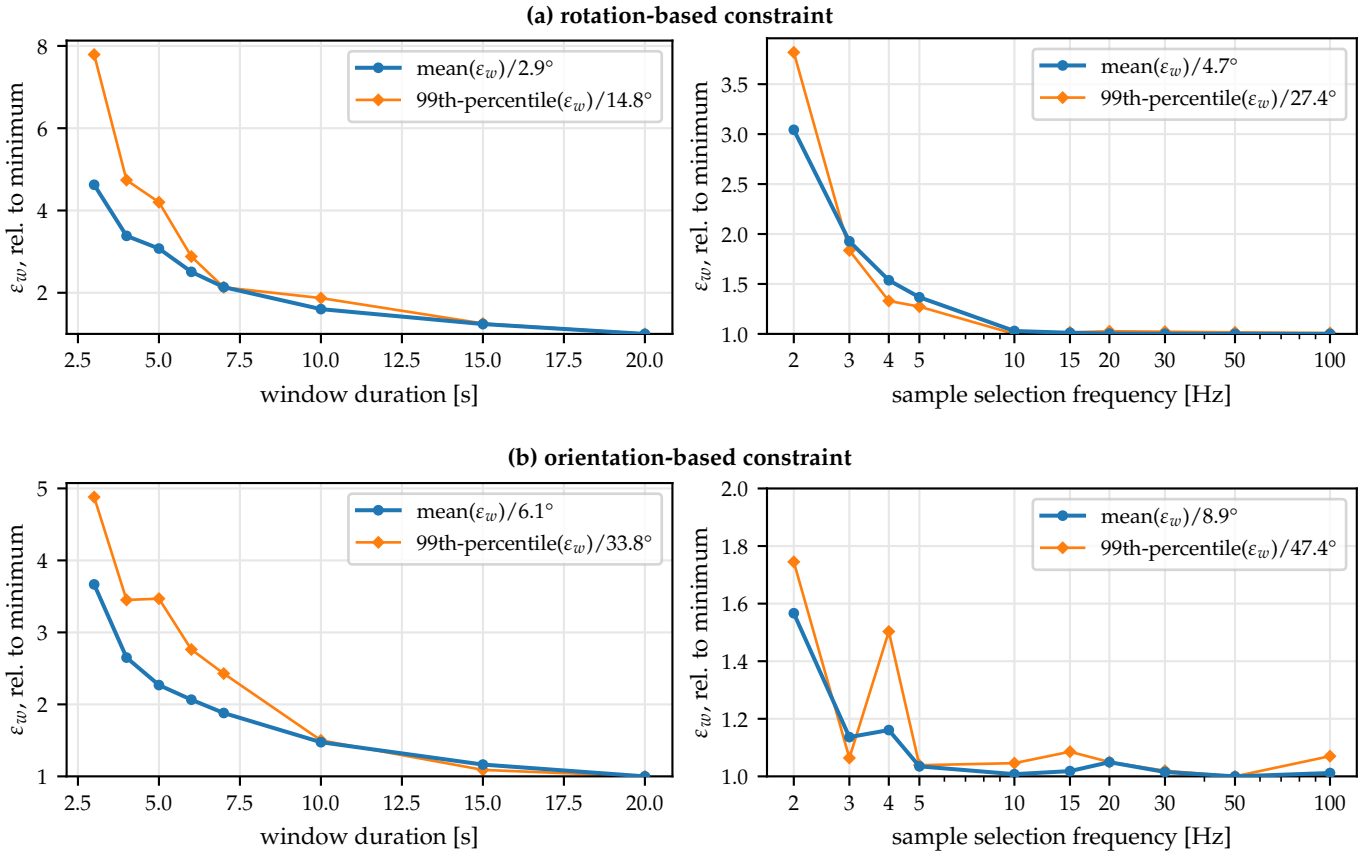

Figure A2. Variability of the obtained axis estimates (mean and 99th-percentile of ε_w, relative to minimum value) for different values of the window duration and the sample selection frequency for the **(a)** rotation-based constraint and the **(b)** orientation-based constraint. In general, using more data (long windows at high sampling rates) leads to more consistent estimates but increases inconvenience for the subject and processing time.

References

1. Picerno, P. 25 Years of Lower Limb Joint Kinematics by Using Inertial and Magnetic Sensors: A Review of Methodological Approaches. *Gait & Posture* **2017**, *51*, 239–246. https://doi.org/10.1016/j.gaitpost.2016.11.008.
2. Filippeschi, A.; Schmitz, N.; Miezal, M.; Bleser, G.; Ruffaldi, E.; Stricker, D. Survey of Motion Tracking Methods Based on Inertial Sensors: A Focus on Upper Limb Human Motion. *Sensors* **2017**, *17*, 1257. https://doi.org/10.3390/s17061257.
3. Vitali, R.V.; Perkins, N.C. Determining Anatomical Frames via Inertial Motion Capture: A Survey of Methods. *Journal of Biomechanics* **2020**, *106*, 109832. https://doi.org/10.1016/j.jbiomech.2020.109832.
4. Seel, T.; Raisch, J.; Schauer, T. IMU-based Joint Angle Measurement for Gait Analysis. *Sensors* **2014**, *14*, 6891–6909. https://doi.org/10.3390/s140406891.
5. Olsson, F.; Kok, M.; Seel, T.; Halvorsen, K. Robust Plug-and-Play Joint Axis Estimation Using Inertial Sensors. *Sensors* **2020**, *20*, 3534. https://doi.org/10.3390/s20123534.
6. Müller, P.; Bégin, M.A.; Schauer, T.; Seel, T. Alignment-Free, Self-Calibrating Elbow Angles Measurement Using Inertial Sensors. *IEEE Journal of Biomedical and Health Informatics* **2017**, *21*, 312–319. https://doi.org/10.1109/JBHI.2016.2639537.
7. Laidig, D.; Schauer, T.; Seel, T. Exploiting Kinematic Constraints to Compensate Magnetic Disturbances When Calculating Joint Angles of Approximate Hinge Joints from Orientation Estimates of Inertial Sensors. In Proceedings of the 2017 International Conference on Rehabilitation Robotics (ICORR), 2017, pp. 971–976. https://doi.org/10.1109/ICORR.2017.8009375.
8. Graurock, D.; Schauer, T.; Seel, T. Automatic Pairing of Inertial Sensors to Lower Limb Segments – a Plug-and-Play Approach. *Current Directions in Biomedical Engineering* **2016**, *2*, 715–718. https://doi.org/10.1515/cdbme-2016-0155.
9. Zimmermann, T.; Taetz, B.; Bleser, G. IMU-to-segment Assignment and Orientation Alignment for the Lower Body Using Deep Learning. *Sensors* **2018**, *18*, 302. https://doi.org/10.3390/s18010302.
10. Seel, T.; Schauer, T.; Raisch, J. Joint Axis and Position Estimation from Inertial Measurement Data by Exploiting Kinematic Constraints. In Proceedings of the 2012 IEEE International Conference on Control Applications, 2012, pp. 45–49. https://doi.org/10.1109/CCA.2012.6402423.

11. Crabolu, M.; Pani, D.; Raffo, L.; Cereatti, A. Estimation of the Center of Rotation Using Wearable Magneto-Inertial Sensors. *Journal of Biomechanics* **2016**, *49*, 3928–3933. https://doi.org/10.1016/j.jbiomech.2016.11.046.
12. Olsson, F.; Halvorsen, K. Experimental Evaluation of Joint Position Estimation Using Inertial Sensors. In Proceedings of the 2017 20th International Conference on Information Fusion (Fusion), 2017, pp. 1–8. https://doi.org/10.23919/ICIF.2017.8009669.
13. Brennan, A.; Deluzio, K.; Li, Q. Assessment of Anatomical Frame Variation Effect on Joint Angles: A Linear Perturbation Approach. *Journal of Biomechanics* **2011**, *44*, 2838–2842. https://doi.org/10.1016/j.jbiomech.2011.09.006.
14. Fan, B.; Li, Q.; Tan, T.; Kang, P.; Shull, P.B. Effects of IMU Sensor-to-Segment Misalignment and Orientation Error on 3-D Knee Joint Angle Estimation. *IEEE Sensors Journal* **2022**, *22*, 2543–2552. https://doi.org/10.1109/JSEN.2021.3137305.
15. Miezal, M.; Taetz, B.; Bleser, G. On Inertial Body Tracking in the Presence of Model Calibration Errors. *Sensors* **2016**, *16*, 1132. https://doi.org/10.3390/s16071132.
16. Bouvier, B.; Duprey, S.; Claudon, L.; Dumas, R.; Savescu, A. Upper Limb Kinematics Using Inertial and Magnetic Sensors: Comparison of Sensor-to-Segment Calibrations. *Sensors* **2015**, *15*, 18813–18833. https://doi.org/10.3390/s150818813.
17. Picerno, P.; Cereatti, A.; Cappozzo, A. Joint Kinematics Estimate Using Wearable Inertial and Magnetic Sensing Modules. *Gait & Posture* **2008**, *28*, 588–595. https://doi.org/10.1016/j.gaitpost.2008.04.003.
18. Picerno, P.; Caliandro, P.; Iacovelli, C.; Simbolotti, C.; Crabolu, M.; Pani, D.; Vannozzi, G.; Reale, G.; Rossini, P.M.; Padua, L.; et al. Upper Limb Joint Kinematics Using Wearable Magnetic and Inertial Measurement Units: An Anatomical Calibration Procedure Based on Bony Landmark Identification. *Scientific Reports* **2019**, *9*, 14449. https://doi.org/10.1038/s41598-019-50759-z.
19. Vargas-Valencia, L.S.; Elias, A.; Rocon, E.; Bastos-Filho, T.; Frizera, A. An IMU-to-body Alignment Method Applied to Human Gait Analysis. *Sensors* **2016**, *16*, 2090. https://doi.org/10.3390/s16122090.
20. Robert-Lachaine, X.; Mecheri, H.; Larue, C.; Plamondon, A. Accuracy and Repeatability of Single-Pose Calibration of Inertial Measurement Units for Whole-Body Motion Analysis. *Gait & Posture* **2017**, *54*, 80–86. https://doi.org/10.1016/j.gaitpost.2017.02.029.
21. Butt, H.T.; Taetz, B.; Musahl, M.; Sanchez, M.A.; Murthy, P.; Stricker, D. Magnetometer Robust Deep Human Pose Regression with Uncertainty Prediction Using Sparse Body Worn Magnetic Inertial Measurement Units. *IEEE Access* **2021**, *9*, 36657–36673. https://doi.org/10.1109/ACCESS.2021.3062545.
22. van der Straaten, R.; Wesseling, M.; Jonkers, I.; Vanwanseele, B.; Bruijnes, A.K.B.D.; Malcorps, J.; Bellemans, J.; Truijen, J.; Baets, L.D.; Timmermans, A. Discriminant Validity of 3D Joint Kinematics and Centre of Mass Displacement Measured by Inertial Sensor Technology during the Unipodal Stance Task. *PLOS ONE* **2020**, *15*, e0232513. https://doi.org/10.1371/journal.pone.0232513.
23. Palermo, E.; Rossi, S.; Marini, F.; Patanè, F.; Cappa, P. Experimental Evaluation of Accuracy and Repeatability of a Novel Body-to-Sensor Calibration Procedure for Inertial Sensor-Based Gait Analysis. *Measurement* **2014**, *52*, 145–155. https://doi.org/10.1016/j.measurement.2014.03.004.
24. Favre, J.; Aissaoui, R.; Jolles, B.M.; de Guise, J.A.; Aminian, K. Functional Calibration Procedure for 3D Knee Joint Angle Description Using Inertial Sensors. *Journal of Biomechanics* **2009**, *42*, 2330–2335. https://doi.org/10.1016/j.jbiomech.2009.06.025.
25. de Vries, W.H.K.; Veeger, H.E.J.; Cutti, A.G.; Baten, C.; van der Helm, F.C.T. Functionally Interpretable Local Coordinate Systems for the Upper Extremity Using Inertial & Magnetic Measurement Systems. *Journal of Biomechanics* **2010**, *43*, 1983–1988. https://doi.org/10.1016/j.jbiomech.2010.03.007.
26. Luinge, H.J.; Veltink, P.H.; Baten, C.T.M. Ambulatory Measurement of Arm Orientation. *Journal of Biomechanics* **2007**, *40*, 78–85. https://doi.org/10.1016/j.jbiomech.2005.11.011.
27. Cutti, A.G.; Giovanardi, A.; Rocchi, L.; Davalli, A.; Sacchetti, R. Ambulatory Measurement of Shoulder and Elbow Kinematics through Inertial and Magnetic Sensors. *Medical & Biological Engineering & Computing* **2008**, *46*, 169–178. https://doi.org/10.1007/s11517-007-0296-5.
28. Ligorio, G.; Bergamini, E.; Truppa, L.; Guaitolini, M.; Raggi, M.; Mannini, A.; Sabatini, A.M.; Vannozzi, G.; Garofalo, P. A Wearable Magnetometer-Free Motion Capture System: Innovative Solutions for Real-World Applications. *IEEE Sensors Journal* **2020**, pp. 1–1. https://doi.org/10.1109/JSEN.2020.2983695.
29. Favre, J.; Jolles, B.M.; Aissaoui, R.; Aminian, K. Ambulatory Measurement of 3D Knee Joint Angle. *Journal of Biomechanics* **2008**, *41*, 1029–1035. https://doi.org/10.1016/j.jbiomech.2007.12.003.
30. Lebleu, J.; Gosseye, T.; Detrembleur, C.; Mahaudens, P.; Cartiaux, O.; Penta, M. Lower Limb Kinematics Using Inertial Sensors during Locomotion: Accuracy and Reproducibility of Joint Angle Calculations with Different Sensor-to-Segment Calibrations. *Sensors* **2020**, *20*, 715. https://doi.org/10.3390/s20030715.
31. Mascia, G.; Brasiliano, P.; Di Feo, P.; Cereatti, A.; Camomilla, V. A Functional Calibration Protocol for Ankle Plantar-Dorsiflexion Estimate Using Magnetic and Inertial Measurement Units: Repeatability and Reliability Assessment. *Journal of Biomechanics* **2022**, p. 111202. https://doi.org/10.1016/j.jbiomech.2022.111202.
32. Cottam, D.S.; Campbell, A.C.; Davey, P.C.; Kent, P.; Elliott, B.C.; Alderson, J.A. Functional Calibration Does Not Improve the Concurrent Validity of Magneto-Inertial Wearable Sensor-Based Thorax and Lumbar Angle Measurements When Compared with Retro-Reflective Motion Capture. *Medical & Biological Engineering & Computing* **2021**. https://doi.org/10.1007/s11517-021-02440-9.
33. Cordillet, S.; Bideau, N.; Bideau, B.; Nicolas, G. Estimation of 3D Knee Joint Angles during Cycling Using Inertial Sensors: Accuracy of a Novel Sensor-to-Segment Calibration Procedure Based on Pedaling Motion. *Sensors* **2019**, *19*, 2474. https://doi.org/10.3390/s19112474.

34. Carcreff, L.; Payen, G.; Grouvel, G.; Massé, F.; Armand, S. Three-Dimensional Lower-Limb Kinematics from Accelerometers and Gyroscopes with Simple and Minimal Functional Calibration Tasks: Validation on Asymptomatic Participants. *Sensors* **2022**, *22*, 5657. https://doi.org/10.3390/s22155657.
35. Salehi, S.; Bleser, G.; Reiss, A.; Stricker, D. Body-IMU Autocalibration for Inertial Hip and Knee Joint Tracking. In Proceedings of the Proceedings of the 10th EAI International Conference on Body Area Networks; ICST (Institute for Computer Sciences, Social-Informatics and Telecommunications Engineering): ICST, Brussels, Belgium, Belgium, 2015; BodyNets '15, pp. 51–57. https://doi.org/10.4108/eai.28-9-2015.2261522.
36. McGrath, T.; Fineman, R.; Stirling, L. An Auto-Calibrating Knee Flexion-Extension Axis Estimator Using Principal Component Analysis with Inertial Sensors. *Sensors* **2018**, *18*, 1882. https://doi.org/10.3390/s18061882.
37. McGrath, T.; Stirling, L. Body-Worn IMU Human Skeletal Pose Estimation Using a Factor Graph-Based Optimization Framework. *Sensors* **2020**, *20*, 6887. https://doi.org/10.3390/s20236887.
38. McGrath, T.; Stirling, L. Body-Worn IMU-based Human Hip and Knee Kinematics Estimation during Treadmill Walking. *Sensors* **2022**, *22*, 2544. https://doi.org/10.3390/s22072544.
39. Olsson, F.; Seel, T.; Lehmann, D.; Halvorsen, K. Joint Axis Estimation for Fast and Slow Movements Using Weighted Gyroscope and Acceleration Constraints. In Proceedings of the 2019 22th International Conference on Information Fusion (FUSION), 2019, pp. 1–8. https://doi.org/10.23919/FUSION43075.2019.9011409.
40. Nowka, D.; Kok, M.; Seel, T. On Motions That Allow for Identification of Hinge Joint Axes from Kinematic Constraints and 6D IMU Data. In Proceedings of the 2019 18th European Control Conference (ECC), 2019. https://doi.org/10.23919/ECC.2019.8795846.
41. Taetz, B.; Bleser, G.; Miezal, M. Towards Self-Calibrating Inertial Body Motion Capture. In Proceedings of the 2016 19th International Conference on Information Fusion (FUSION), 2016, pp. 1751–1759.
42. Norden, M.; Müller, P.; Schauer, T. Real-Time Joint Axes Estimation of the Hip and Knee Joint during Gait Using Inertial Sensors. In Proceedings of the Proceedings of the 5th International Workshop on Sensor-based Activity Recognition and Interaction; Association for Computing Machinery: New York, NY, USA, 2018; iWOAR '18, pp. 1–6. https://doi.org/10.1145/3266157.3266213.
43. de Vries, W.H.K.; Veeger, H.E.J.; Baten, C.T.M.; van der Helm, F.C.T. Magnetic Distortion in Motion Labs, Implications for Validating Inertial Magnetic Sensors. *Gait & Posture* **2009**, *29*, 535–541. https://doi.org/10.1016/j.gaitpost.2008.12.004.
44. Wu, G.; van der Helm, F.C.T.; Veeger, H.E.J.D.; Makhsous, M.; Roy, P.V.; Anglin, C.; Nagels, J.; Karduna, A.R.; McQuade, K.; Wang, X.; et al. ISB Recommendation on Definitions of Joint Coordinate Systems of Various Joints for the Reporting of Human Joint Motion—Part II: Shoulder, Elbow, Wrist and Hand. *Journal of Biomechanics* **2005**, *38*, 981–992. https://doi.org/10.1016/j.jbiomech.2004.05.042.
45. Kuipers, J.B. Quaternions and Rotation Sequences. In Proceedings of the Proceedings of the International Conference on Geometry, Integrability and Quantization; Coral Press Scientific Publishing: Varna, Bulgaria, 1999; pp. 127–143. https://doi.org/10.7546/giq-1-2000-127-143.
46. Laidig, D.; Müller, P.; Seel, T. Automatic Anatomical Calibration for IMU-based Elbow Angle Measurement in Disturbed Magnetic Fields. *Current Directions in Biomedical Engineering* **2017**, *3*, 167–170. https://doi.org/10.1515/cdbme-2017-0035.
47. Laidig, D.; Seel, T. VQF: Highly Accurate IMU Orientation Estimation with Bias Estimation and Magnetic Disturbance Rejection. *Information Fusion* **2023**, *91*, 187–204. https://doi.org/10.1016/j.inffus.2022.10.014.
48. Laidig, D.; Lehmann, D.; Bégin, M.A.; Seel, T. Magnetometer-Free Realtime Inertial Motion Tracking by Exploitation of Kinematic Constraints in 2-DoF Joints. In Proceedings of the 2019 41st Annual International Conference of the IEEE Engineering in Medicine and Biology Society (EMBC), 2019, pp. 1233–1238. https://doi.org/10.1109/EMBC.2019.8857535.
49. Wright, S.; Nocedal, J. Numerical Optimization. *Springer Science* **1999**, *35*, 67–68.
50. Weygers, I.; Kok, M.; Seel, T.; Shah, D.; Taylan, O.; Scheys, L.; Hallez, H.; Claeys, K. In-Vitro Validation of Inertial-Sensor-to-Bone Alignment. *Journal of Biomechanics* **2021**, p. 110781. https://doi.org/10.1016/j.jbiomech.2021.110781.
51. Dam, E.B.; Koch, M.; Lillholm, M. *Quaternions, Interpolation and Animation*; Vol. 2, Datalogisk Institut, Københavns Universitet Copenhagen, 1998.